J. Fluid Mech. (2024), *vol*. 987, A10, doi:10.1017/jfm.2024.390

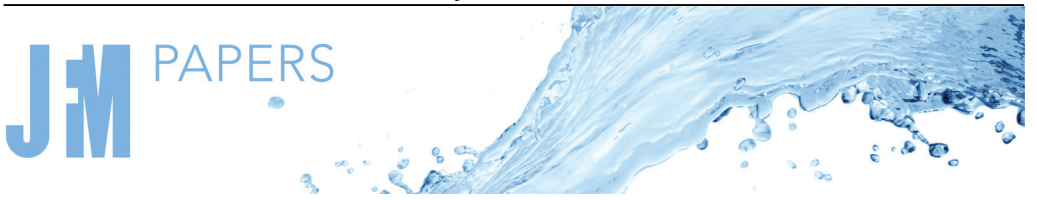

Freeze-out of perturbation growth for shocked heavy fluid layers by eliminating reverberating waves

Zhouyang Cong[1], **Xu Guo**[1,†], **Zhangbo Zhou**[1], **Wan Cheng**[1] **and Ting Si**[1]

[1]Department of Modern Mechanics, University of Science and Technology of China, Hefei 230026, PR China

(Received 7 January 2024; revised 14 April 2024; accepted 14 April 2024)

The shock wave accelerating a heavy fluid layer can induce reverberating waves that continuously interact with the first and second interfaces. In order to manipulate the perturbation growths at fluid-layer interfaces, we present a theoretical framework to eliminate the reverberating waves. A model is established to predict the individual freeze-out (i.e. stagnation of perturbation growth) for the first and second interfaces under specific flow conditions determined based on the shock dynamics theory. The theoretical model quantifies the controllable parameters required for freeze-out, including the initial amplitudes of the first and second interfaces, the interface coupling strength and the maximum initial layer thickness preventing the second interface's phase reversal. The effectiveness of the model in predicting individual freeze-out for the first and second interfaces is validated numerically over a wide range of initial conditions. The upper and lower limits of initial amplitudes for the freeze-out of the whole fluid-layer width growth are further predicted. Within this amplitude range, a slightly higher initial amplitude for the second interface is specified, effectively arresting the growth of the entire fluid-layer width before the phase reversal of the second interface.

Key words: shock waves

1. Introduction

Richtmyer–Meshkov instability (RMI) occurs when an impulsive acceleration (e.g. a shock wave) is imposed on a perturbed fluid interface with different densities (Richtmyer 1960; Meshkov 1969). Generally, the perturbation at the interface initially grows rapidly, followed by nonlinear growth and formation of interpenetrating structures including bubbles (light fluids penetrating into heavy fluids) and spikes (heavy fluids penetrating into light fluids), eventually leading to transition to turbulence. The RMI plays a significant role

† Email address for correspondence: clguoxu@ustc.edu.cn

in various scientific and engineering applications such as supernova explosions (Kuranz *et al.* 2018), scramjet (Yang, Chang & Bao 2014) and inertial confinement fusion (ICF) (Betti & Hurricane 2016). Particularly, in ICF, the perturbation growth of RMI poses a significant challenge to implosion ignition since it induces undesired mixing between materials in different layers, diminishing the purity of fuels in the capsule and thus leading to reduced fusion yields (Lindl *et al.* 2014; Betti & Hurricane 2016). As a result, the stagnation of perturbation growth of RMI, a phenomenon commonly referred to as freeze-out (Mikaelian 1994), is of importance for ICF, and has been a subject of great interest (Zhou 2017*a*,*b*; Zhou *et al.* 2021).

Most previous studies focused on the single-interface freeze-out, which can be achieved by two shock impacts. The essence of this type of freeze-out is that the vorticity induced by the second shock offsets the counterpart induced by the first shock, resulting in stagnation of perturbation growth. Mikaelian (1985) first proposed this idea and summarized the schemes for freeze-out. For a heavy/light interface with completed phase reversal, the second shock propagates in the same direction as the first shock. For a heavy/light interface with incomplete phase reversal or a light/heavy interface, the second shock propagates in the opposite direction to the first shock. Charakhch'yan (2000, 2001) numerically achieved freeze-out for a heavy/light single-mode interface by adjusting the intensity of the second shock. For a light/heavy single-mode interface, the freeze-out of perturbation growth was achieved numerically by Mikaelian (2010) and experimentally by Chen *et al.* (2023*b*). Note that the second impact required for freeze-out can also be provided by rarefaction waves. Chen *et al.* (2023*a*) experimentally investigated the evolution of a heavy/light single-mode interface successively impacted by a shock and reflected rarefaction waves. It was shown that the freeze-out of perturbation growth emerges when the rarefaction waves impact the interface at a suitable time after the interface's phase reversal.

The ICF capsule consists of multiple material layers (Terry, Perkins & Sepke 2012; Montgomery *et al.* 2018) and thus freeze-out of perturbation growth for fluid layers is significant. For a finite-thickness fluid layer, the growth of perturbations on one interface can affect that of the other, which causes the well-known phenomenon of interface coupling or feedthrough (Mikaelian 1983; Jacobs *et al.* 1995; Desjardins *et al.* 2019). If a reasonable condition is satisfied, the coupling effect induced by the first interface can freeze the growth of perturbations on the second interface, and *vice versa*. By considering the coupling effect between the two interfaces, Mikaelian (1995) derived the freeze-out condition for perturbation growth of an A/B/A-type fluid layer, where 'A' and 'B' stand for the fluids outside and inside the fluid layer, respectively. Later, Mikaelian (1996) examined the freeze-out model through numerical simulations and found that the freeze-out did not occur as predicted by his theory. The deviation can be attributed to two reasons. First, the model of Mikaelian (1995) does not take into account the effects caused by shock compression. This leads to the model's inability to correctly characterize the parameters required for freeze-out. Second, reverberating waves within the layer continually interact with fluid-layer interfaces, resulting in additional Rayleigh–Taylor effects and stretching effects (Liang *et al.* 2020; Cong *et al.* 2022), thereby causing the freeze-out theory of Mikaelian (1995) to be invalid. In other words, the presence of reverberating waves makes it difficult to achieve freeze-out for fluid-layer interfaces by interface coupling alone since, even if the interface coupling leads to freeze-out of perturbation growth, the reverberating waves would destroy the freeze-out state.

Note that if the reverberating waves within the fluid layer provide vorticity with an opposite sign to the original vorticity on the interface, they contribute to the freeze-out of perturbation growth. As a consequence, by reasonably matching the effects of interface coupling and reverberating waves, freeze-out for fluid-layer interfaces can be achieved. Based on this, Liang & Luo (2023) numerically studied the evolution of a fluid layer with two heavy/light interfaces on both sides, and found that the perturbation growth of the first or second interface can be frozen under the combined effects of interface coupling and reverberating waves. Notably, the initial conditions for freeze-out are stringent in the work of Liang & Luo (2023), since these two effects need to be elaborately regulated to achieve freeze-out. Additionally, a low incident shock Mach number was considered in this work (Liang & Luo 2023) so that only the first interaction between the reverberating waves and the fluid-layer interfaces plays a significant role in freeze-out. However, for a relatively strong incident shock, the second and even later interactions between the reverberating waves and the fluid-layer interfaces become significant (Zhang *et al.* 2022). This would complicate the matching of the effects of interface coupling and reverberating waves to achieve freeze-out, because the interaction of later reverberating waves with the interface can destroy the freeze-out state established by the combined effects of interface coupling and the earlier reverberating wave. In short, achieving freeze-out of perturbation growth for fluid layers remains challenging, which motivates the present work.

In this work, freeze-out for a heavy fluid layer is investigated both theoretically and numerically. The heavy fluid layer has been a commonly considered configuration in previous studies, and the evolution mechanism for this type of fluid layer has been extensively studied (Jacobs *et al.* 1993, 1995; Balakumar *et al.* 2008, 2012; Balasubramanian, Orlicz & Prestridge 2013; Orlicz *et al.* 2015; Liang *et al.* 2020; Cong *et al.* 2022). Nevertheless, exploration involving freeze-out of perturbation growth for the heavy fluid layer is limited (Mikaelian 1995, 1996). Owing to the unfavourable effect of reverberating waves on freeze-out in most cases, we propose to eliminate the reverberating waves within the heavy fluid layer to realize freeze-out. In the absence of reverberating waves, the interface coupling dominates the freeze-out for fluid-layer interfaces, reducing the complexity of theoretical modelling. By reasonably characterizing the initial parameters required for freeze-out, we establish a freeze-out theory for heavy-fluid-layer interfaces. Significantly, a relatively high Mach number of 2 will be employed in the current study, posing a greater challenge for freeze-out compared with the previous fluid-layer study with a lower Mach number of 1.24 (Liang & Luo 2023). The remainder of this paper is organized as follows. Section 2 describes the method for eliminating reverberating waves and the freeze-out theory. Section 3 presents the numerical methods used for simulating the shock–interface interactions. In § 4, parametric studies are conducted to examine the validity of the freeze-out theory. Section 5 investigates the simultaneous freeze-out for both the first and second interfaces, and it also explores the freeze-out for the entire fluid-layer width growth. Finally, conclusions are presented.

2. Theoretical analysis

We will first introduce the method of eliminating reverberating waves within the heavy fluid layer, as described in § 2.1. Then, a theory for predicting the individual freeze-out for the first and second interfaces is established in § 2.2. Since freeze-out for the second interface must be achieved prior to the phase reversal, a model, as the supplementary condition for the second interface's freeze-out, is established in § 2.3.

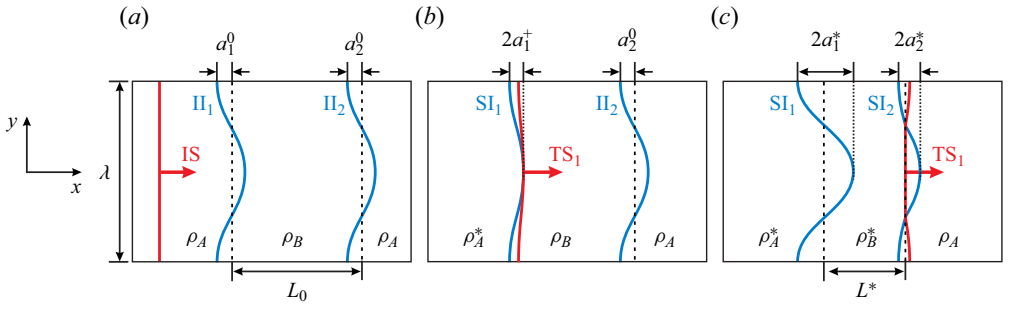

Figure 1. Schematics of a heavy fluid layer ($\rho_B > \rho_A$) for the shock compression in the absence of reverberating waves. (*a*) The moment ($t < 0$) before the arrival of the incident shock IS. (*b*) The moment ($t = t^+$) when the transmitted shock TS$_1$ just leaves the first interface. (*c*) The moment ($t = t^*$) when the shock TS$_1$ reaches the middle position of the initial second interface. Here, II$_1$ and II$_2$ denote the initial first and second interfaces, respectively; SI$_1$ and SI$_2$ denote the shocked first and second interfaces, respectively; a_1^0 and a_2^0 denote initial amplitudes of the first and second interfaces, respectively; a_1^+ denotes the amplitude of the first interface at t^+; a_1^* and a_2^* denote the amplitudes of the first and second interfaces at t^*, respectively; L_0 denotes the initial layer thickness; L^* denotes the layer thickness at t^*; λ denotes the interface wavelength; and ρ_A and ρ_B (ρ_A^* and ρ_B^*) denote the pre-shock (post-shock) densities for fluid A and fluid B, respectively.

2.1. *Method of eliminating reverberating waves*

Figure 1(*a*) illustrates the initial configuration of the A/B/A-type heavy fluid layer with sinusoidal interfaces on both sides. Here, a_1^0 and a_2^0 denote the initial amplitudes of the first and second interfaces, respectively; L_0 denotes the initial fluid-layer thickness; λ denotes the initial wavelength of the fluid-layer interface; and ρ_A and ρ_B denote initial densities for fluid A and fluid B, respectively. Notably, the initial amplitudes of both perturbed interfaces satisfy the small-amplitude hypothesis in this work, i.e. $ka_1^0 \ll 1$ and $ka_2^0 \ll 1$, where k ($= 2\pi/\lambda$) is the wavenumber. For the small-amplitude scenario, the method of eliminating reverberating waves, derived based on one-dimensional (1-D) shock dynamics theories (Han & Yin 1993), is considered to be applicable.

As shown in figure 1(*a*), when the incident shock IS propagates from fluid A to fluid B, total transmission (i.e. no reflected wave) occurs at the first interface, provided that the following condition (Han & Yin 1993) is satisfied:

$$c_B/c_A = \kappa, \tag{2.1}$$

with

$$\kappa = \frac{\gamma_B\left[1 + \dfrac{\gamma_B + 1}{2\gamma_B}(p_2/p_1 - 1)\right]^{1/2}}{\gamma_A\left[1 + \dfrac{\gamma_A + 1}{2\gamma_A}(p_2/p_1 - 1)\right]^{1/2}}, \tag{2.2}$$

where c_B/c_A is the ratio of sound speed in fluid B to that in fluid A; γ_A and γ_B are the adiabatic indices for fluid A and fluid B, respectively; and p_2/p_1 is the ratio of pressure behind IS to that in front of IS, which can be expressed as

$$p_2/p_1 = 1 + \frac{2\gamma_A}{\gamma_A + 1}(M_s^2 - 1), \tag{2.3}$$

with M_s denoting the incident shock Mach number. By substituting $c_A = \sqrt{\gamma_A p_A/\rho_A}$ and $c_B = \sqrt{\gamma_B p_B/\rho_B}$ into (2.1) and simplifying, we obtain

$$1 + \frac{2}{p_2/p_1 - 1} = \frac{\rho_B - \rho_A}{\gamma_A \rho_A - \gamma_B \rho_B}. \tag{2.4}$$

Substituting (2.3) into (2.4) yields

$$R_0 = \frac{\rho_B}{\rho_A} = \frac{\gamma_A(\gamma_A + 1)M_s^2}{\gamma_B - \gamma_A + \gamma_A(\gamma_B + 1)M_s^2}, \tag{2.5}$$

where R_0 is the initial density ratio. Equation (2.5) gives the relationship among R_0, M_s, ρ_A, ρ_B, γ_A and γ_B under the total transmission condition.

When the IS passes through the first interface, the transmitted shock TS_1 is generated, as depicted in figure 1(*b*). Due to the total transmission of IS at the first interface, the value of p_2/p_1 remains equal for both IS and TS_1. As a result, the gas parameters on both sides of the second interface also satisfy (2.4), that is, TS_1 is also totally transmissive at the second interface. Here, it can be concluded that, for an A/B/A-type heavy fluid layer, if the shock is totally transmissive at the first interface, it is also totally transmissive at the second interface. The total transmission at both fluid-layer interfaces causes the post-shock flow velocity to remain unvaried. As a consequence, the shock-induced jump velocities for the first and second interfaces are equal. In the remainder of this paper, the parameter ΔU will be used to represent the jump velocity for both the first and second interfaces under the total transmission condition.

2.2. *Theory of individual freeze-out for the first and second interfaces*

The freeze-out theory for heavy fluid layers focuses on the case where the first and second interfaces are in phase, as illustrated in figure 1(*a*). This choice is limited by the fact that freeze-out only theoretically emerges for in-phase cases (Mikaelian 1995). To construct the freeze-out theory, we need to know the parameters (including the density ratio, the fluid-layer thickness and the interface amplitudes) at the initiation of interface coupling. For the shock-accelerated fluid layer, the interface coupling is initiated after the shock compression. Figure 1 shows schematics of the shock-compression process for the heavy fluid layer in the absence of reverberating waves. The time when the incident shock IS just contacts the first interface is defined as $t = 0$. When the IS completely passes through the first interface ($t = t^+$), as shown in figure 1(*b*), the density of fluid A changes from ρ_A to ρ_A^*, and the first interface amplitude is compressed from a_1^0 to a_1^+. When the transmitted shock TS_1 reaches the second interface centre ($t = t^*$), as shown in figure 1(*c*), the fluid-layer thickness is compressed from L_0 to the minimum value of L^*, the amplitude of the first interface changes to a_1^* and the amplitude of the second interface is compressed from a_2^0 to a_2^*. In this work, the interface coupling is considered to be initiated at $t = t^*$. Then, the post-shock quantities at $t = t^*$, including the density ratio R^*, the layer thickness L^* and the interface amplitudes a_1^* and a_2^*, required for the establishment of the freeze-out theory, will be determined.

By solving the 1-D Riemann problem of the shock–interface interaction, the post-shock densities ρ_A^* and ρ_B^* can be obtained and thus R^* can be written as

$$R^* = \rho_B^*/\rho_A^*. \tag{2.6}$$

The duration of the whole compression process of the fluid layer can be denoted as L_0/V_{ts1}, where V_{ts1} represents the velocity of TS_1. Throughout this period, the downstream

movement of the first interface can be quantified as $\Delta U(L_0/V_{ts1})$. As a result, L^* can be written as

$$L^* = L_0 - \Delta U(L_0/V_{ts1}) = L_0(1 - \Delta U/V_{ts1}). \tag{2.7}$$

Notably, under the total transmission condition, L^* remains unvaried since the jump velocities for both interfaces are equal.

The development of the first interface's amplitude during the transition from a_1^0 to a_1^* can be divided into two stages: (I), $0 < t \leqslant t^+$, the shock-compression stage; (II), $t^+ < t \leqslant t^*$, the independent perturbation growth stage. In stage I, the amplitude (a_1^+) after shock compression can be expressed as

$$a_1^+ = a_1^0(1 - \Delta U/V_{is}), \tag{2.8}$$

where V_{is} is the velocity of IS. In stage II, the amplitude growth for the first interface initially enters a startup period. According to the work of Lombardini & Pullin (2009), the amplitude growth rate of the first interface in the startup period can be expressed as

$$\frac{\mathrm{d}a_1}{\mathrm{d}t} = \frac{C_1\Gamma}{\Delta UA^+}\dot{a}_1^{Rich}\frac{t}{\tau}. \tag{2.9}$$

Here, τ is the startup time, which can be found using

$$\tau = \frac{1}{2k}\left(\frac{1 - A^+}{V_f + \Delta U} + \frac{1 + A^+}{V_{ts1} - \Delta U}\right), \tag{2.10}$$

where $A^+ = (\rho_B^* - \rho_A^*)/(\rho_B^* + \rho_A^*)$ is the post-shock Atwood number, and V_f is the velocity of the reflected wave from the interface. In the total transmission condition, V_f is considered to be equal to the local sound velocity. The parameter Γ is the circulation imposed by IS on the first interface (Samtaney & Zabusky 1994), which can be expressed as

$$\Gamma = \frac{c_A}{M_s}\left[\frac{\gamma_B(1 - \phi(p_3/p_1, \gamma_B))}{\gamma_A(\gamma_B - 1)R_0} - \frac{1 - \phi(p_3/p_2, \gamma_A)\phi(p_2/p_1, \gamma_A)}{\gamma_A - 1}\right], \tag{2.11}$$

with

$$\phi(\xi, \eta) \equiv \xi\frac{(\eta - 1)\xi + \eta + 1}{(\eta + 1)\xi + \eta - 1}, \tag{2.12}$$

where p_3 is the pressure behind TS_1. Here, $C_1 = [(1 - A^+)(V_f + \Delta U) - (1 + A^+)(-V_{ts1} + \Delta U)]/(V_f + V_{ts1})$ and $\dot{a}_1^{Rich}$ is the perturbation growth rate obtained from the model of Richtmyer (1960) as

$$\dot{a}_1^{Rich} = ka_1^+\Delta UA^+. \tag{2.13}$$

After the startup period, the amplitude growth for the first interface enters a linear period. The amplitude growth rate in this period can be given by (2.13).

Notably, at $t = t^*$, the amplitude growth of the first interface can be categorized into two scenarios: (i) for $t^* - t^+ \leq \tau$, the amplitude growth is still in the startup period; (ii) for $t^* - t^+ > \tau$, the amplitude growth has entered the linear period. By integrating the time

term in (2.9) and (2.13), the amplitude a_1^* in the two scenarios can be expressed as

$$a_1^* = \begin{cases} a_1^+ + \dfrac{C_1 \Gamma \dot{a}_1^{Rich}}{2\Delta U \tau A^+}(t^* - t^+)^2, & t^* - t^+ \le \tau; \\ a_1^+ + \dfrac{C_1 \Gamma \dot{a}_1^{Rich}}{2\Delta U A^+}\tau + \dot{a}_1^{Rich}(t^* - t^+ - \tau), & t^* - t^+ > \tau. \end{cases} \tag{2.14}$$

The amplitude a_2^* can be expressed as

$$a_2^* = \frac{a_2^0 + a_2^+}{2}, \tag{2.15}$$

where a_2^+ is the amplitude for the second interface at the time when TS_1 completely passes through it. The a_2^+ can be expressed as

$$a_2^+ = a_2^0(1 - \Delta U / V_{ts1}). \tag{2.16}$$

In the previous studies involving a heavy/light single-mode case (Meyer & Blewett 1972; Holmes *et al.* 1999; Guo *et al.* 2022*a*), a_2^*, rather than a_2^+, is employed as the post-shock amplitude for theoretical modelling since a_2^* performs better in predicting the amplitude growth rate for the heavy/light configuration. In the current work, a_2^* is also selected as the post-shock amplitude of the second interface to establish the freeze-out theory.

By replacing the pre-shock quantities R_0, L_0, a_1^0 and a_2^0 in the model of Mikaelian (1995) with the post-shock quantities R^*, L^*, a_1^* and a_2^*, we can obtain the following expression to predict the freeze-out for the first interface:

$$a_1^* = a_2^* \sin\theta', \tag{2.17}$$

and the following expression to predict the freeze-out for the second interface:

$$a_2^* = a_1^* \sin\theta'. \tag{2.18}$$

In (2.17) and (2.18), θ' is the coupling angel with consideration of the post-shock quantities R^* and L^* and

$$\sin\theta' = \frac{2W}{1 + W^2}, \tag{2.19}$$

with

$$W = 1 + \sinh(kL^*)\tanh\left(\frac{kL^*}{2}\right) + \frac{\sinh(kL^*)}{R^*}\left\{1 + \left[1 + R^{*2} + 2R^*\coth(kL^*)\right]^{1/2}\right\}. \tag{2.20}$$

When employing equation (2.17) to forecast the first interface's freeze-out, we find that the calculated value of a_1^* is too large, resulting in a significant amplitude growth rate of the first interface. As a result, the coupling effect imposed by the second interface fails to freeze the amplitude growth of the first interface. Similarly, (2.18) also yields an overestimation of a_2^*, leading to its inability to predict the freeze-out for the second interface. The failure of (2.17) and (2.18) indicates that considering only the modification of post-shock quantities for the original model of Mikaelian (1995) is insufficient.

It should be noted that, in the original model of Mikaelian (1995), R_0 and L_0 are independent parameters. However, in the total transmission condition, R_0 is determined by (2.5), establishing a relationship between R_0 and the adiabatic indices (γ_A and γ_B).

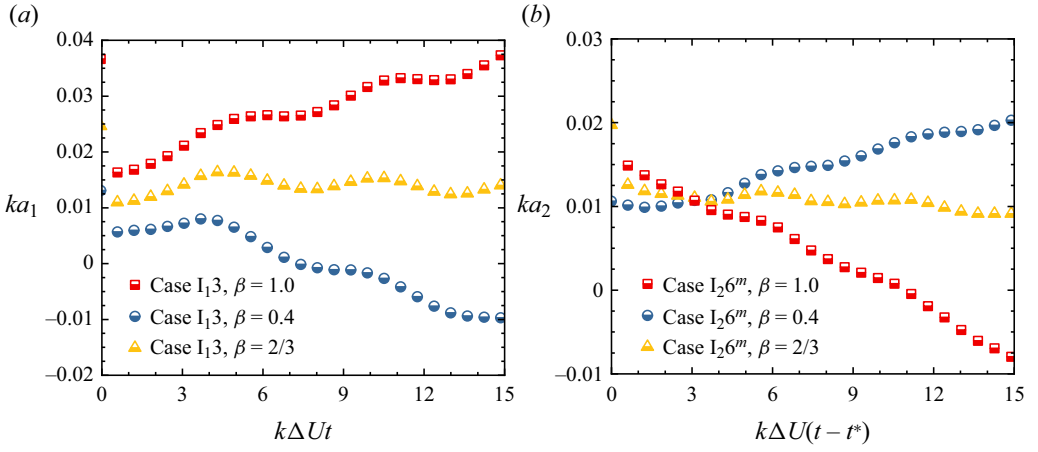

Figure 2. The dimensionless amplitude growth for the first (*a*) and second (*b*) interfaces predicted by the freeze-out theory with different β values. Cases I_13 and I_26^m are designed for examining the freeze-out for the first and second interfaces, respectively, with their initial conditions detailed in tables 1 and 2 in §§ 4.2 and 4.3.

Any change in R_0 requires γ_A or γ_B to change accordingly to ensure total transmission. Nevertheless, based on the shock dynamics theory (Han & Yin 1993), variations in γ_A or γ_B can affect the values of ΔU and V_{ts1}, thus influencing the value of L^* (see (2.7)). Consequently, under the total transmission condition, changes in R_0 can lead to variations in L^* so that R^* and L^* are not independent. It is believed that directly substituting the independent parameters L_0 and R_0 with the dependent parameters L^* and R^* into (2.19) causes it to be incapable of accurately quantifying the interface coupling strength required for freeze-out, thus leading to the failure of (2.17) and (2.18). To account for additional effects arising from the correlation between R^* and L^*, an empirical parameter β is introduced in (2.19), resulting in a modified form of (2.19):

$$\sin\theta^* = \frac{2\beta W}{1 + W^2}, \tag{2.21}$$

where θ^* is the modified coupling angle.

Then, we describe the determination process of the parameter β. As mentioned above, (2.17) and (2.18) yield an overestimation for a_1^* and a_2^*, respectively, resulting in their inability to predict the individual freeze-out for the first and second interfaces. As a consequence, to ensure the effectiveness of the freeze-out theory, it is necessary to introduce a parameter less than 1 to multiply $\sin\theta'$ in (2.17) to reduce the resulting value of a_1^*, and in (2.18) to reduce the resulting value of a_2^*. In other words, the parameter β introduced should be smaller than 1. Naturally, β is expected to be a constant, representing the simplest approach for the modification. To determine the optimal value for β, we explore some values within the range of 0 to 1. For each attempted β value, numerical simulations are conducted to confirm whether freeze-out occurs. Using cases I_13 and I_26^m (details provided in tables 1 and 2 in §§ 4.2 and 4.3) as examples, figure 2(*a*,*b*) shows the dimensionless amplitude growth of the first and second interfaces predicted by the freeze-out theory with three β values ($\beta = 1$, 0.4 and 2/3). It is evident that, for β values that are either too large ($\beta = 1$) or too small ($\beta = 0.4$), the amplitude growth of both interfaces remains unfrozen. However, when $\beta = 2/3$, the amplitude growth of the first and second interfaces is effectively arrested. Importantly, this β value ($= 2/3$) is found to be effective for the freeze-out theory in predicting freeze-out for the first and second

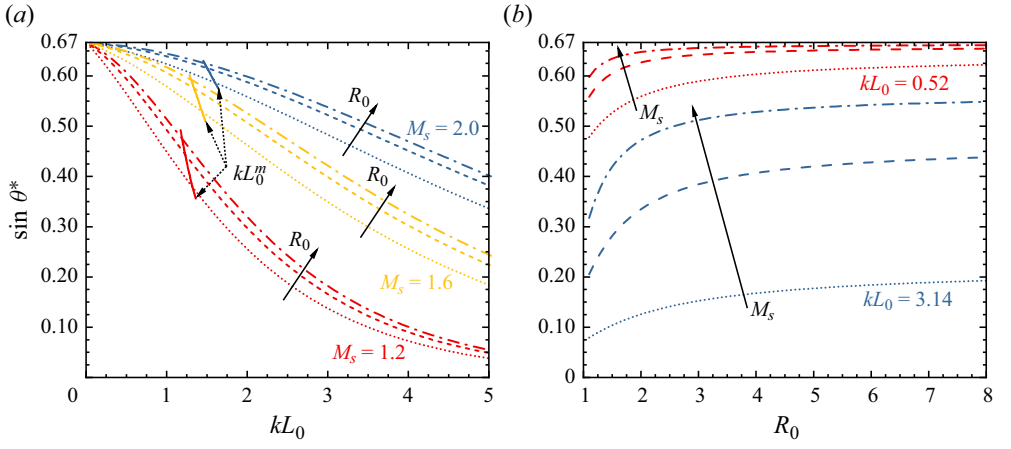

Figure 3. Variations of $\sin\theta^*$ as a function of kL_0 (*a*) and R_0 (*b*). In (*a*), the values of R_0 corresponding to each M_s are 2, 3 and 4, respectively. In (*b*), the values of M_s corresponding to each kL_0 are 1.2, 1.6 and 2.0, respectively. The lines for kL_0^m are obtained based on (2.27), as described in § 2.3.

interfaces over a broad range of initial conditions, as observed in figures 8 and 11 in §§ 4.2 and 4.3. Consequently, $\beta = 2/3$ is recommended in (2.21).

Notably, $\sin\theta^*$ varies from 0 to 2/3. As the value of $\sin\theta^*$ becomes larger, the interface coupling strength is higher. To illustrate the dependence of $\sin\theta^*$ on initial conditions, figure 3 presents the variations of $\sin\theta^*$ vs kL_0 and R_0, with consideration of the influence of M_s. As shown in figure 3(*a*), as kL_0 decreases, $\sin\theta^*$ increases and when kL_0 approaches zero, $\sin\theta^*$ converges to 2/3. As shown in figure 3(*b*), as R_0 increases, $\sin\theta^*$ increases but saturates rapidly. Particularly, at a relatively large kL_0 such as $kL_0 = 3.14$, increasing R_0 alone cannot make $\sin\theta^*$ converge to 2/3. As a result, enhancing of the interface coupling strength is more effectively achieved by reducing kL_0 rather than increasing R_0. In addition, as M_s increases, $\sin\theta^*$ also increases. This phenomenon occurs because a stronger shock impact leads to a greater compression in both interface thicknesses and fluid densities, resulting in an increase in both kL^* and R^* and, consequently, an increase in $\sin\theta^*$.

Finally, with consideration of the quantity $\sin\theta^*$, the model for predicting the freeze-out for the first interface can be expressed as

$$a_1^* = a_2^* \sin\theta^*, \tag{2.22}$$

and the model for predicting the freeze-out for the second interface can be expressed as

$$a_2^* = a_1^* \sin\theta^*. \tag{2.23}$$

Equations (2.22) and (2.23) quantify the amplitudes of the first and second interfaces at the onset of interface coupling, as well as the interface coupling strength required for freeze-out.

Based on the variations of the first and second interfaces' amplitudes during the shock compression stage, the initial amplitudes (a_1^0 and a_2^0) of the first and second interfaces required for freeze-out can be determined. For instance, we can first set a value for a_1^0, and then, the a_2^0 required for freeze-out for the first interface can be determined by combining (2.22), (2.8), (2.14), (2.15) and (2.16); and the a_2^0 required for freeze-out for the second interface can be determined by combining (2.23), (2.8), (2.14), (2.15) and (2.16).

2.3. *Supplementary condition for the second interface's freeze-out*

After the shock impact, phase reversal generally arises at the second interface of the heavy fluid layer (Meyer & Blewett 1972). Previous fluid-layer studies have indicated that, once phase reversal of the second interface is accomplished, the spike continually grows downstream so that freeze-out cannot be achieved by the interface coupling (Liang *et al.* 2020; Cong *et al.* 2022). Consequently, the freeze-out for the second interface needs to be achieved before phase reversal. This indicates that (2.23) is not sufficient to achieve the freeze-out for the second interface.

After the shock passes through the fluid layer ($t > t^*$), the coupling effect is considered to propagate at the local sound velocity (c_B^*) within the fluid layer. The value of c_B^* can be obtained by the shock dynamics theory (Han & Yin 1993). As the first interface evolves, its induced coupling effects continuously transmit to the second interface. If the first interface imposes sufficient coupling effects on the second interface, the second interface's phase reversal could be prevented (Liang & Luo 2023). The coupling transfer time (t^{ct}) between the first and second interfaces is expressed as

$$t^{ct} = L^*/c_B^*. \tag{2.24}$$

Note that, as the initial layer thickness increases, the t^{ct} becomes larger. Consequently, over the same time interval, the total amount of coupling effects imposed on the second interface decreases with increasing initial layer thickness. As a result, there is a maximum initial layer thickness (L_0^m) at which the total coupling effects imposed on the second interface just prohibit the second interface's phase reversal.

Starting from t^*, the phase-reversal time (t^{pr}) for the second interface is given by

$$t^{pr} = \frac{a_2^0}{V_{ts1}} + \frac{a_2^+}{\dot{a}_2^{Rich}}, \tag{2.25}$$

where $\dot{a}_2^{Rich}$ ($= ka_2^+\Delta UA^+$) is the amplitude growth rate in the phase reversal stage (Zhai *et al.* 2016). To prevent phase reversal at the second interface, t^{ct} should be smaller than t^{pr}. This leads to the relation

$$t^{ct} = \delta t^{pr}, \tag{2.26}$$

where $\delta \in (0, 1)$ is a proportional factor. Combining (2.26) with (2.7), the maximum initial layer thickness L_0^m is expressed as

$$L_0^m = \frac{\delta c_B^*}{1 - \Delta U/V_{ts1}}\left(\frac{1}{k\Delta UA^+} + \frac{a_2^0}{V_{ts1}}\right). \tag{2.27}$$

When $L_0 < L_0^m$, the phase reversal at the second interface can be prevented so that the freeze-out for the second interface is feasible.

In (2.27), only the factor δ is unknown. To determine δ, we perform numerical simulations with various initial conditions. Specifically, eight numerical cases, $\mathrm{I}_2 4^m$–$\mathrm{I}_2 6^m$ and $\mathrm{I}_2 9^m$–$\mathrm{I}_2 13^m$, each with unique initial conditions detailed in table 2 in § 4.3, are considered. For each case, simulations with different initial layer thicknesses are conducted to specify the numerical maximum initial layer thickness ($L_0^{m,num}$) that prevents the phase reversal at the second interface. Then, by substituting the $L_0^{m,num}$ values into (2.27), eight numerical values for δ are obtained. It is shown that each case yields a distinct numerical value for δ, indicating that a unified δ cannot be determined. In other words, δ is influenced by the initial conditions, much like t^{ct} and t^{pr}. Here, $\sin\theta^*$, a non-dimensional

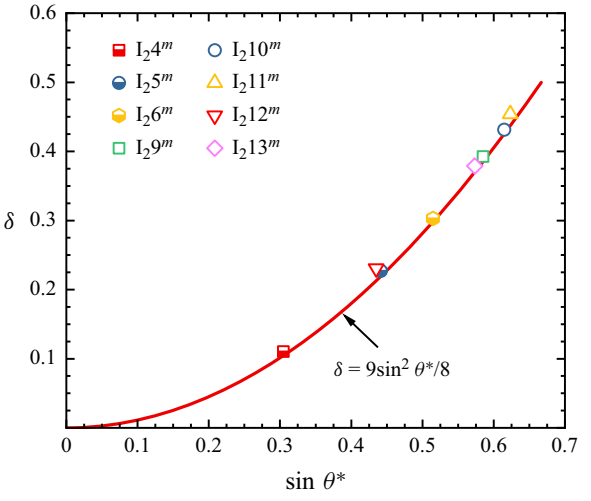

Figure 4. The variations of δ with $\sin\theta^*$. Symbols denote the numerical values of δ, obtained from simulations of cases I_24^m–I_26^m and I_29^m–I_213^m. The initial conditions of the eight numerical cases are presented in table 2. The red line indicates the quadratic function, $\delta = 9\sin^2\theta^*/8$.

parameter dependent on initial conditions, is employed to specify δ. Figure 4 shows the δ–$\sin\theta^*$ plot. It is observed that, as $\sin\theta^*$ increases, δ also increases. We find that a quadratic function, $\delta = 9\sin^2\theta^*/8$, can well characterize the relationship between δ and $\sin\theta^*$. As a result, $\delta = 9\sin^2\theta^*/8$ is recommended for defining δ. Notably, $\sin\theta^*$ varies from 0 to 2/3 so that δ varies from 0 to 1/2. Consequently, as illustrated in (2.26), the maximum value of the coupling transfer time t^{ct} must be less than 1/2 of the phase reversal time t^{pr} to prevent the second interface's phase reversal.

The theoretical lines of the dimensionless form of L_0^m, denoted as kL_0^m, are presented in figure 3(*a*). The value for the dimensionless initial layer thickness (kL_0) on the left-hand side of the lines of kL_0^m enables the freeze-out for the second interface. In short, to achieve freeze-out for the second interface, it is essential not only for the amplitudes of the first and second interfaces to satisfy (2.23), but also for the initial layer thickness to remain smaller than L_0^m (i.e. $L_0 < L_0^m$).

3. Numerical methods

3.1. *Numerical set-up and code validation*

The initial configuration of the A/B/A-type heavy fluid layer, adopted in the simulations, is depicted in figure 1(*a*). The detailed settings for the initial parameters including a_1^0, a_2^0, M_s, L_0, ρ_A, ρ_B and λ will be described in §§ 4 and 5. The computational domain's length is set to be at least ten times half the wavelength λ (in this work, three different wavelengths with values of 120, 240 and 480 mm are considered) to avoid interference of reflected waves from the right boundary with the evolving interface during the designated simulation time. To optimize computational efficiency, calculations are performed only for half the computational domain along the y-direction. In the simulations, the nodes with a volume fraction of fluid B between 5 % and 95 % are considered as the interface. The amplitude of the evolving first (second) interface, denoted as a_1 (a_2), is defined as half of

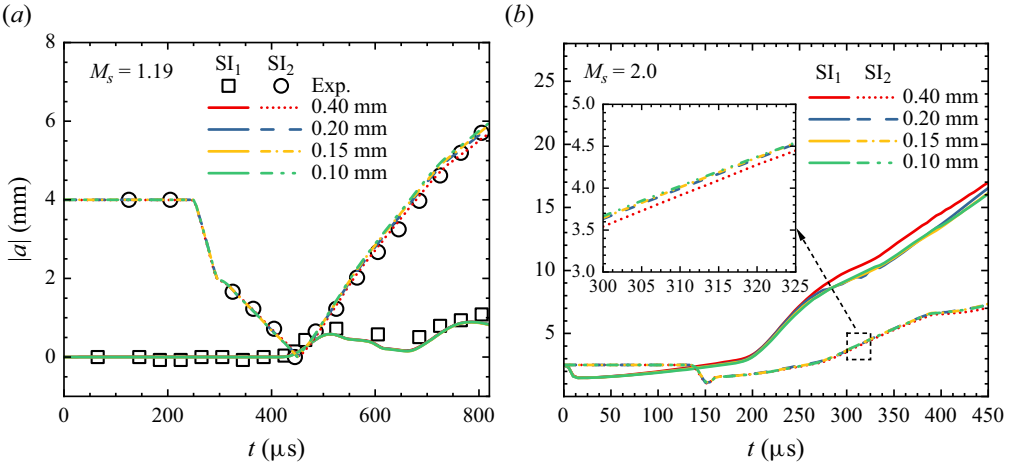

Figure 5. Code validation based on amplitude growths of heavy-fluid-layer interfaces under the conditions of lower (*a*) and higher (*b*) Mach numbers. Symbols represent experimental results obtained from the air/SF_6/air fluid-layer case in the previous work (Li *et al.* 2023). Lines represent numerical results based on four kinds of mesh sizes.

the distance between the bubble tip and the spike tip at the nodes with a fluid B volume fraction of 50 %. In the simulations, the temperature is 295 K and the pressure is 101.3 kPa.

The interactions between a shock and the heavy fluid layer are described by two-dimensional (2-D) compressible multi-component Euler equations. The optimized six-point weighted compact nonlinear scheme (WCNS) with minimum dispersion and adaptive dissipation (Zhou *et al.* 2023*b*) is used. The optimized WCNS scheme is extended to multi-species flows by incorporating the double-flux algorithm of Abgrall & Karni (2001), and has shown a good capability to simulate RMI problems (Zhou *et al.* 2023*a*). For time integration, a third-order total variation diminishing Runge–Kutta method is adopted. Further details about the numerical scheme can be found in the previous work (Zhou *et al.* 2023*b*).

The experimental data from a shocked air/SF_6/air fluid layer in the previous work (Li *et al.* 2023) are utilized for code validation. The simulation employs identical initial conditions to those used in the experiment. The incident shock Mach number is 1.19. The first interface of the fluid layer is a flat one, while the second interface is a single-mode case with an initial amplitude and wavelength of 4 and 60 mm, respectively. The volume fraction of SF_6 within the layer is 82.6 %, and the surrounding air outside the layer is pure. Figure 5(*a*) shows the comparison of interface amplitude growths between the experimental data and our simulation results. It is found that the experimental and numerical results achieve a good agreement.

To evaluate grid convergence, four different mesh sizes (0.4 mm, 0.2 mm, 0.15 mm and 0.1 mm) are adopted to simulate an air/SF_6/air fluid layer impacted by a shock with $M_s = 2.0$. Figure 5(*b*) shows the temporal amplitude variations for the first and second interfaces for each mesh size at $M_s = 2.0$. Additionally, figure 5(*a*) includes the amplitude growth data of the lower Mach number case, considering these four mesh sizes. It is evident that the amplitude growth data exhibit convergence as the mesh size decreases from 0.4 to 0.1 mm, both for higher and lower Mach number cases. Particularly, the numerical results for cases with mesh sizes of 0.2 mm, 0.15 mm and 0.1 mm are in close agreement. To strike a balance between computational cost and accuracy, a mesh size of

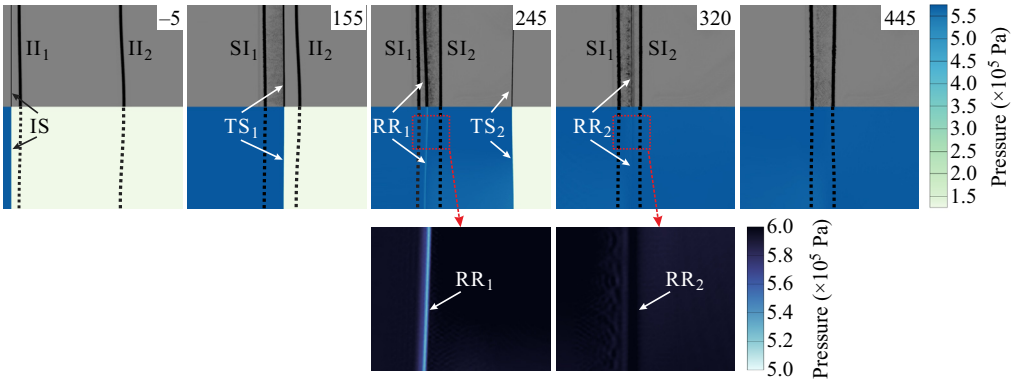

Figure 6. Numerical schlieren images and pressure fields for a shocked heavy-fluid-layer case, designed for examining the total transmission. Note that two partially enlarged views of the pressure fields are provided at the bottom. Here, RR_1 and RR_2 denote the regions consisting of rarefaction and compression waves; II_1 and II_2 denote the initial first and second interfaces, respectively; SI_1 and SI_2 denote the shocked first and second interfaces, respectively, and similarly hereinafter. The black dashed lines in the pressure plots denote a half-wavelength interface, which are intentionally plotted to enhance understanding of the interface evolution. Numbers in the numerical schlieren images denote time with unit of μs.

0.15 mm is utilized for cases with $\lambda = 120$ mm, while a mesh size of 0.2 mm is utilized for cases with $\lambda = 240$ mm or 480 mm.

3.2. *Total transmission validation*

The total transmission of a shock at small-amplitude fluid-layer interfaces is assessed. The initial conditions for the examination are listed as follows: M_s is set to 2.0 to investigate the total transmission at a relatively high Mach number; SF_6 is chosen as the heavy fluid with ρ_B and γ_B of 6.08 kg m^{-3} and 1.10, respectively; R_0 is set to 3, causing ρ_A to be 2.03 kg m^{-3}; γ_A is determined to be 4.72 using (2.5); and a_1^0 and a_2^0 are 0.36 and 1 mm, respectively, both satisfying the small-amplitude hypothesis. Notably, the values of a_1^0 and a_2^0 satisfy (2.22) so that the perturbation growth of the first interface would be frozen. Since the reverberating waves within the layer arise due to reflection from the second interface, only the total transmission at the second interface is examined.

Figure 6 shows the numerical schlieren images and corresponding pressure fields of a shocked SF_6 fluid layer for the examination case. As shown in figure 6, the incident shock IS passes through the first interface, giving rise to the transmitted shock TS_1 (155 μs). Subsequently, TS_1 impacts the second interface, leading to the formation of a transmitted shock TS_2 (245 μs). Notably, a reflected region RR_1 is formed when TS_1 traverses the second interface. The generation of RR_1 region is primarily ascribed to the diffuse initial interface across four grids in this work. Due to the slight diffusion of the interface, the complete satisfaction of the total transmission condition is not achieved, resulting in the generation of reflected waves. Furthermore, the derivation of the total transmission condition is based on 1-D assumptions so that the 2-D small-amplitude perturbation may still give rise to reflected waves. In the partially enlarged view of the pressure plot at 245 μs, as shown in figure 6, the pressure first decreases and then increases when traversing the RR_1 region from left to right. This indicates that the RR_1 region consists of rarefaction and compression waves. These waves in the RR_1 region successively strike the first interface, resulting in an RR_2 region consisting of reflected compression and

rarefaction waves (320 μs). In this examination case, the ratio of the pressure ahead of the RR_1 (RR_2) region to that behind the RR_1 (RR_2) region is 1.0098 (0.9987). We also determine the two pressure ratios for all cases considered in this work (see tables 1–3 for details of the cases), and the pressure ratio involving the RR_1 (RR_2) region varies from 1.0041 (0.9865) to 1.0148 (0.9995) for different cases. This indicates that the reverberating waves resulting from the initial 2-D diffuse interfaces are weak for all cases so that the shock can be considered totally transmissive at the second interface.

Notably, the maximum values of ka_1^0 or ka_2^0 for all cases in this work are no more than 0.1. These initial amplitude values satisfy the small-amplitude requirements of $ka_1^0 \ll 1$ and $ka_2^0 \ll 1$, because the values of $ka_{1,2}^0$ are an order of magnitude smaller than unity. Such a small amplitude can significantly reduce the influence of dimensionality on the total transmission condition. Furthermore, the reverberating waves resulting from the small-amplitude interfaces are very weak. As a result, $ka_{1,2}^0 = 0.1$ may serve as a threshold for the total transmission of a shock at the perturbed fluid-layer interface.

4. Evaluation of the freeze-out theory

In this section, § 4.1 presents the initial condition settings for parametric studies conducted for the freeze-out examination; § 4.2 examines the validity of (2.22) in predicting the freeze-out for the first interface; and § 4.3 examines the validity of (2.23) and (2.27) in predicting the freeze-out for the second interface.

4.1. *Initial condition settings for parametric studies*

Equations (2.22), (2.23) and (2.27) are all functions of $\sin\theta^*$, which is dependent on the incident shock Mach number (M_s), the initial density ratio (R_0), the initial fluid-layer thickness (L_0) and the interface wavelength (λ). As a result, the individual freeze-out for the first and second interfaces under the conditions of various M_s, R_0, L_0 and λ will be examined.

In the previous freeze-out studies with lower Mach numbers ($M_s < 1.4$) (Chen *et al.* 2023*a*,*b*; Liang & Luo 2023), after the incident shock passes through the interface, both the transmitted shock and reflected wave rapidly propagate away from the interface. As a result, after a very short time, there are no large changes in pressure in the vicinity of the interface so that compressibility effects are weak in the lower Mach number cases (Richtmyer 1960). As the Mach number increases, the interface velocity shows a significant rise. For instance, in the cases of $M_s = 2.0$ considered in this work, the velocity (ΔU) of the first interface is approximately 80 % of that (V_{ts1}) of the transmitted shock TS_1. The velocity ratio ($\Delta U/V_{ts1} \approx 0.8$) at $M_s = 2.0$ is much higher than the corresponding ratio ($\Delta U/V_{ts1} \approx 0.4$) at $M_s = 1.2$. As a result, in relatively high Mach number cases, the transmitted shock recedes slowly from the interface (Glendinning *et al.* 2003; Motl *et al.* 2009). This results in changes in pressure behind the transmitted shock influencing the interface perturbation growth for a relatively long time; thus, compressibility effects become significant in higher Mach number cases (Sadot *et al.* 2003; Guo *et al.* 2020; Zhang *et al.* 2022). The presence of compressibility effects adds complexity to the coupling between the two interfaces, possibly influencing the realization of freeze-out. Furthermore, compressibility effects may cause the two models of (2.22) and (2.23) to be invalid in predicting freeze-out, because these two models are initially derived by treating the shock as an instantaneous acceleration on incompressible fluids (Mikaelian 1995). In the present study, to examine the applicability and effectiveness of the models (2.22) and (2.23) under conditions of relatively high Mach numbers, the M_s is

consistently set at 2.0, except for cases specifically designed for freeze-out examinations at lower Mach numbers ($M_s = 1.2$ and 1.6).

We first employ real gases to form different R_0. After examining 56 real gases (see Appendix A for details of the gases), it is found that, under the total transmission condition, the largest R_0 is achieved when xenon (Xe) is used as fluid A and a mixture of decafluorobutane (C_4F_{10}) and neopentane (C_5H_{12}) is used as fluid B. Specifically, at $M_s = 1.2$, 1.6 and 2.0, the largest R_0 under the total transmission condition is determined to be 1.49, 1.40 and 1.36, respectively. Additionally, we consider the following two cases to investigate the potential effect of gas species on the validity of our freeze-out theory: krypton (Kr) is employed as fluid A and a mixture of C_4F_{10} and C_5H_{12} is employed as fluid B; argon (Ar) is employed as fluid A and a mixture of butane (C_4H_{10}) and propane (C_3H_8) is employed as fluid B. At $M_s = 2.0$, the R_0 value for these two cases under the total transmission condition is 1.35 and 1.31, respectively. Further details of the real-gas cases can be found in tables 1 and 2 (denoted as cases $I_1 1$–$I_1 5$ and $I_2 4^m$–$I_2 8^m$). The discussion about the total transmission under real-gas conditions is presented in Appendix A.

Notably, the largest R_0 formed by real gases is no more than 1.49 under the total transmission condition, as M_s varies from 1.2 to 2.0. This density ratio is relatively small, so that it is insufficient for validating the effectiveness of our freeze-out theory from the perspective of R_0. To address this limitation, artificial gases are utilized, providing a convenient means to adjust R_0. In this work, using artificial gases, we form R_0 values with a range of 2–4. The upper limit for R_0 is based on the fact that, beyond $R_0 = 4$, the change in $\sin\theta^*$ is minimal, resulting in a limited variation in interface coupling strength (see figure 3*b*). As illustrated in tables 1 and 2, for cases $I_1 6$–$I_1 14$, cases $I_2 1$–$I_2 3$ and cases $I_2 9^m$–$I_2 15^m$, the artificial gas is utilized as fluid A, and the real gas SF_6 is utilized as fluid B. The properties including ρ_A and γ_A for the artificial gases can be determined by (2.5).

The choice of L_0 involved in parametric studies is made to first ensure that the layer thickness (L^*) at the coupling onset time (t^* in this work) remains under 1/3 of the interface wavelength. This criterion is based on the finding that the interface coupling becomes non-negligible when the layer thickness at the onset time is less than 1/3 of the interface wavelength (Taylor 1950). Particularly, in freeze-out test cases for the second interface, the choice of L_0 is further limited by L_0^m, as described in § 2.3.

In most cases, λ is fixed at 120 mm, which is the same as the transverse size of the shock tube used in our previous work (Cong *et al.* 2022; Guo *et al.* 2022*a*,*b*). To explore potential effects arising from variations in interface wavelengths on freeze-out, we also include two additional wavelengths of 240 and 480 mm. These values, generally unexplored in previous shock-tube studies, offer insights into the impact of different interface wavelengths on the freeze-out phenomenon.

Notably, (2.22) and (2.23) are derived based on the small-amplitude hypothesis (i.e. $ka_1^0 \ll 1$ and $ka_2^0 \ll 1$). As a result, the initial amplitudes of all cases in this work are set in accordance with this condition. When freeze-out for the first interface is examined, a_2^0 is first specified, and then the corresponding a_1^0 is determined by combining (2.15), (2.22), (2.14) and (2.8). When freeze-out for the second interface is examined, a_1^0 is first specified, and then the corresponding a_2^0 is determined by combining (2.8), (2.14), (2.23) and (2.15). For all cases, ka_1^0 has a range of 0.0084–0.0628, and ka_2^0 has a range of 0.0162–0.0628.

Case	M_s	L_0	R_0	λ	a_1^0	a_2^0	$\sin\theta^*$	ΔU	ρ_A	γ_A	ρ_B	γ_B
$I_1$1	1.2	21.5	1.49	120	0.39	1.0	0.379	48.3	5.47	1.68	8.14	1.05
$I_1$2	1.6	39.2	1.40	120	0.44	1.0	0.397	128.4	5.47	1.68	7.65	1.06
$I_1$3	2.0	60	1.36	120	0.48	1.0	0.413	197.6	5.47	1.68	7.44	1.06
$I_1$4	2.0	60	1.35	120	0.47	1.0	0.403	247.4	3.49	1.67	4.70	1.07
$I_1$5	2.0	60	1.31	120	0.43	1.0	0.375	358.4	1.66	1.67	2.18	1.11
$I_1$6	2.0	20	3	120	0.67	1.0	0.637	254.8	2.03	4.72	6.08	1.10
$I_1$7	2.0	60	3	120	0.36	1.0	0.512	254.8	2.03	4.72	6.08	1.10
$I_1$8	2.0	100	3	120	0.16	1.0	0.366	254.8	2.03	4.72	6.08	1.10
$I_1$9	2.0	60	2	120	0.39	1.0	0.472	239.4	3.04	2.89	6.08	1.10
$I_1$10	2.0	60	4	120	0.35	1.0	0.529	262.4	1.52	6.56	6.08	1.10
$I_1$11	1.2	20.7	3	120	0.40	1.0	0.475	66.5	2.03	3.81	6.08	1.10
$I_1$12	1.6	39.4	3	120	0.34	1.0	0.501	169.2	2.03	4.41	6.08	1.10
$I_1$13	2.0	120	3	240	1.18	2.4	0.512	254.8	2.03	4.72	6.08	1.10
$I_1$14	2.0	240	3	480	2.35	4.8	0.512	254.8	2.03	4.72	6.08	1.10
S1	2.0	—	3	120	0.36	—	—	254.8	2.03	4.72	6.08	1.10

Table 1. Initial conditions of cases $I_1$1–$I_1$14 designed for testing the validity of (2.22) in predicting freeze-out for the first interface. Case S1 is a single-mode case, which is utilized for comparison. In cases $I_1$1–$I_1$3, fluid A is Xe. In cases I_4 and I_5, fluid A is Kr and Ar, respectively. In cases $I_1$1–$I_1$4, fluid B is a mixture of C_4F_{10} and C_5H_{12}, and the volume fractions of C_4F_{10} and C_5H_{12} in cases $I_1$1–$I_1$4 are 74.39 % and 25.61 %, 67.30 % and 32.70 %, 64.31 % and 35.69 %, 24.58 % and 75.42 %. In case $I_1$5, fluid B is a mixture of C_4H_{10} and C_3H_8, and the volume fractions of C_4H_{10} and C_3H_8 are 59.80 % and 40.20 %. In cases $I_1$6–$I_1$14, fluid B is SF_6, and fluid A is the artificial gas whose ρ_A and γ_A are determined by (2.5) to satisfy the total transmission condition. For cases $I_1$1–$I_1$3, the selection of L_0 results in the same L^*, and similarly, for cases $I_1$7, $I_1$11-$I_1$12. The purpose of maintaining the same L^* is to emphasize the effect of the Mach number. The units of L_0, λ, a_1^0 and a_2^0 are mm, the unit of ΔU is $\mathrm{m\,s^{-1}}$ and the unit of ρ_A and ρ_B is $\mathrm{kg\,m^{-3}}$.

4.2. *Freeze-out for the first interface*

Cases $I_1$1–$I_1$3 and $I_1$11–$I_1$12, cases $I_1$6–$I_1$8, cases $I_1$1–$I_1$5 and $I_1$9–$I_1$10 and cases $I_1$13–$I_1$14, with their initial conditions summarized in table 1, are designed to examine the validity of (2.22) in predicting the freeze-out for the first interface from the perspectives of M_s, L_0, R_0 and λ, respectively. The inclusion of different gases in these cases also offers an opportunity to assess the validity of (2.22) from the perspective of the gas species. Additionally, case S1, as a single-mode scenario, is included for comparison. As illustrated in table 1, all values of a_1^0 determined by our freeze-out theory are smaller than the values of a_2^0.

Case $I_1$7 is taken as an example to illustrate the interface evolution observed in cases $I_1$1–$I_1$12, all featuring an identical wavelength of 120 mm. Figure 7(*a*) presents the numerical schlieren images of interface evolution for case $I_1$7. Notably, numbers in images of figure 7(*a*) denote the dimensionless time ($k\Delta Ut$). The fluid layer in case $I_1$7 first experiences a compression process resulting from the IS impact. Then, phase reversal of the second interface occurs after the impact of TS_1 ($k\Delta Ut = 1.9$–6.3). Note that, at $k\Delta Ut = 6.3$, the first interface's morphology remains almost unchanged compared with its post-shock state ($k\Delta Ut = 1.9$). This phenomenon occurs because the second interface has a higher initial amplitude and thus a faster amplitude growth rate (Richtmyer 1960; Meyer & Blewett 1972) in comparison with the first interface. As a result, after phase reversal, the upstream growth of the second interface's bubble effectively squeezes the bubble of the first interface, hindering its evolution. As time elapses, the second interface constantly develops so that it imposes a stronger squeeze on the first interface. In a late

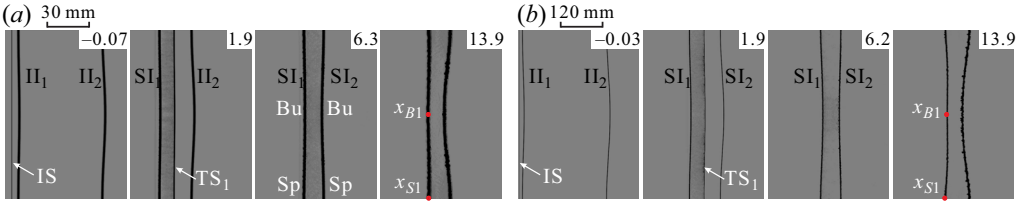

Figure 7. Numerical schlieren images of interface evolution for cases $I_1 7$ (*a*) and $I_1 14$ (*b*). Here, 'Bu' and 'Sp' denote bubbles and spikes, respectively, and 'x_{B1}' and 'x_{S1}' denote the tips of bubbles and spikes for the first interface, respectively. Numbers denote the dimensionless time $k\Delta Ut$.

stage ($k\Delta Ut = 13.9$), the coupling effect from the second interface even causes the bubble tip of the first interface to slightly protrude upstream, further impeding the first interface's evolution.

Case $I_1 14$ is taken as an example to illustrate the interface evolution observed in cases $I_1 13$–$I_1 14$, featuring larger interface wavelengths of 240 and 480 mm, respectively. Figure 7(*b*) presents the interface evolution for case $I_1 14$. It is observed that, at a late stage ($k\Delta Ut = 13.9$), the bubble tip in case $I_1 14$ becomes nearly flat but remains downstream of the spike tip, which is different from the observation in case $I_1 7$. The distinction arises primarily from the larger initial amplitude and greater initial layer thickness in case $I_1 14$. When subjected to the coupling effect of the second interface, the larger initial amplitude requires more time for the bubble tip of the first interface to move upstream of the spike tip. Moreover, the greater layer thickness allows for a longer transfer time of coupling effect from the second interface, thus delaying movement of the bubble tip at the first interface. As a result, the bubble tip of the first interface in case $I_1 14$ is more prone to remain downstream of the spike tip compared with case $I_1 7$.

The dimensionless amplitude growth of the first interface for cases $I_1 1$–$I_1 14$ is shown in figure 8, in which the time is scaled as $k\Delta Ut$ and the amplitude is scaled as ka_1. The amplitude a_1 for the evolving first interface is defined as $(x_{B1} - x_{S1})/2$, where x_{B1} and x_{S1} denote positions of the bubble tip and the spike tip for the first interface, respectively (see figure 7). It is observed that the amplitude data for cases $I_1 13$–$I_1 14$ do not collapse with those for cases $I_1 1$–$I_1 12$. This is primarily because the initial amplitudes for cases $I_1 13$-$I_1 14$ are larger than those for cases $I_1 1$–$I_1 12$, resulting in consistently higher evolving amplitude data for these two cases. Notably, the amplitude data for cases with higher L_0, R_0 and M_s (such as cases $I_1 7$–$I_1 8$, $I_1 10$, $I_1 13$–$I_1 14$) exhibit oscillations, which are attributed to the reflected rarefaction and compression waves from the 2-D diffuse interface, as detailed in § 3.2. The effect of the rarefaction waves leads to an increase in amplitude for the first interface, while compression waves contribute to a decrease, resulting in the oscillatory amplitude growth. As L_0 decreases, the period of the oscillation shortens; and as R_0 and M_s decrease, the strength of the reverberating waves diminishes. Consequently, the oscillation is not evident for the cases with smaller values of L_0, R_0 and M_s.

Overall, the amplitude growths of the first interface for cases $I_1 1$–$I_1 14$ are roughly frozen, as illustrated in figure 8. This indicates that the model (2.22) is robust in predicting freeze-out for the first interface over a relatively wide range of initial conditions. Furthermore, (2.22) shows insensitivity to variations in M_s, R_0, L_0, λ and gas species.

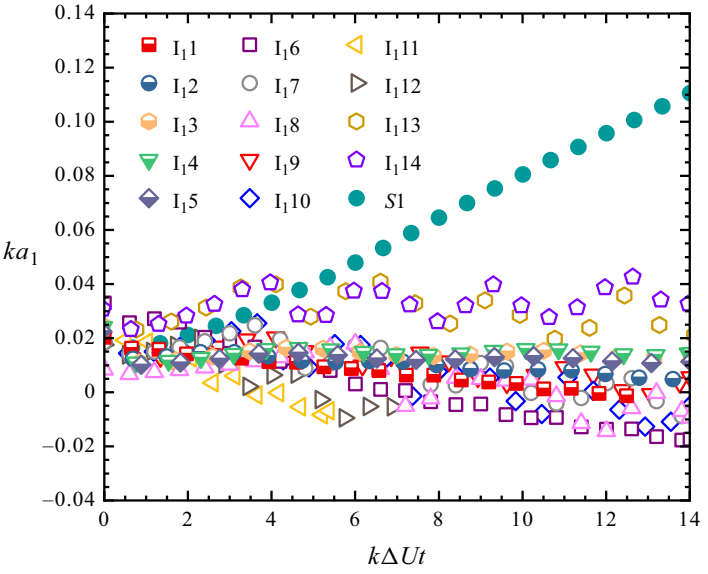

Figure 8. Temporal variations of the first interface's amplitudes for cases $I_1 1$–$I_1 14$ in a dimensionless form. Case S1 is a single-mode case included for comparison.

4.3. *Freeze-out for the second interface*

First, the influence of whether the second interface accomplishes phase reversal on the prediction of (2.23) is examined. Case $I_2 1$, with $L_0 = 20$ mm, is designed as an incomplete phase-reversal scenario, and cases $I_2 2$ and $I_2 3$, with $L_0 = 35$ and 60 mm, are designed as completed phase-reversal scenarios. The selection of L_0 values for cases $I_2 1$–$I_2 3$ is based on the value of L_0^m, which is calculated as 28.7 mm using (2.27). Further details of the initial conditions for cases $I_2 1$–$I_2 3$ are presented in table 2. The numerical schlieren images of the interface evolution for cases $I_2 1$–$I_2 3$ are shown in figure 9. For case $I_2 1$ with a smaller L_0, as shown in figure 9(*a*), the bubble tip of the first interface constantly squeezes that of the second interface and even occupies the position where the bubble tip of the second interface would be, thus preventing phase reversal of the second interface. Conversely, for cases $I_2 2$ and $I_2 3$ with a larger L_0, as shown in figure 9(*b*,*c*), phase reversal of the second interface is completed.

The dimensionless amplitude growth of the second interface for cases $I_2 1$–$I_2 3$ is presented in figure 10, in which the time is scaled as $k\Delta U(t - t^*)$ and the amplitude is scaled as ka_2. The amplitude a_2 for the evolving second interface is defined as $(x_{B2} - x_{S2})/2$, where x_{B2} and x_{S2} denote positions of the bubble tip and the spike tip for the second interface, respectively (see figure 9). It is evident that the amplitude growth of the second interface for case $I_2 1$ is frozen, while the two phase-reversal cases display continuous negative perturbation growth. This indicates that although (2.23) defines the relationship between a_1^0 and a_2^0, freeze-out for the second interface cannot be achieved once phase reversal is accomplished.

Second, the validity of (2.23) in predicting freeze-out for the second interface at $L_0 = L_0^m$ is examined. Cases $I_2 4^m$–$I_2 6^m$ and $I_2 12^m$–$I_2 13^m$, cases $I_2 4^m$–$I_2 11^m$ and cases $I_2 14^m$–$I_2 15^m$, with the initial conditions presented in table 2, are designed to examine the second interface's freeze-out from the perspectives of M_s, R_0 and λ, respectively. Figure 11 shows the dimensionless amplitude growths of the second interface in cases $I_2 4^m$–$I_2 15^m$. Given that cases $I_2 9^m$–$I_2 15^m$ have larger initial amplitudes in comparison

Case	M_s	L_0 (L_0^m)	R_0	λ	a_1^0	a_2^0	$\sin\theta^*$	ΔU	ρ_A	γ_A	ρ_B	γ_B
I_21	2.0	20	3	120	1.0	0.78	0.637	254.8	2.03	4.72	6.08	1.10
I_22	2.0	35	3	120	1.0	0.74	0.597	254.8	2.03	4.72	6.08	1.10
I_23	2.0	60	3	120	1.0	0.71	0.512	254.8	2.03	4.72	6.08	1.10
I_24^m	1.2	28.0	1.49	120	1.0	0.31	0.310	48.3	5.47	1.68	8.14	1.05
I_25^m	1.6	32.0	1.40	120	1.0	0.38	0.445	128.4	5.47	1.68	7.65	1.06
I_26^m	2.0	36.7	1.36	120	1.0	0.39	0.516	197.6	5.47	1.68	7.44	1.06
I_27^m	2.0	36.8	1.35	120	1.0	0.39	0.508	247.4	3.49	1.67	4.70	1.07
I_28^m	2.0	37.1	1.31	120	1.0	0.36	0.485	358.4	1.66	1.67	2.18	1.11
I_29^m	2.0	30.6	2	120	1.0	0.42	0.586	239.4	3.04	2.89	6.08	1.10
I_210^m	2.0	28.7	3	120	1.0	0.76	0.615	254.8	2.03	4.72	6.08	1.10
I_211^m	2.0	28.1	4	120	1.0	0.81	0.624	262.4	1.52	6.56	6.08	1.10
I_212^m	1.2	23.5	3	120	1.0	0.51	0.443	66.5	2.03	3.81	6.08	1.10
I_213^m	1.6	25.6	3	120	1.0	0.69	0.575	169.2	2.03	4.41	6.08	1.10
I_214^m	2.0	56.2	3	240	2.4	1.86	0.617	254.8	2.03	4.72	6.08	1.10
I_215^m	2.0	112.4	3	480	4.8	3.72	0.617	254.8	2.03	4.72	6.08	1.10
S2	2.0	—	3	120	—	0.76	—	254.8	2.03	4.72	6.08	1.10

Table 2. Initial conditions for cases I_21–I_23, I_24^m–I_215^m and S2. Cases I_21–I_23 are designed for examining the influence of whether the second interface completes phase reversal on the predictions of (2.23). Cases I_24^m–I_215^m are designed for testing the validity of (2.23) and (2.27) in predicting freeze-out for the second interface. The superscript 'm' denotes that L_0 of the cases is calculated using (2.27). Case S2 is a single-mode case, which is utilized for comparison. In cases I_24^m–I_26^m, fluid A is Xe. In cases I_27^m and I_28^m, fluid A is Kr and Ar, respectively. In cases I_24^m–I_27^m, fluid B is a mixture of C_4F_{10} and C_5H_{12}, and the volume fractions of C_4F_{10} and C_5H_{12} in cases I_24^m–I_27^m are 74.39 % and 25.61 %, 67.30 % and 32.70 %, 64.31 % and 35.69 %, 24.58 % and 75.42 %. In case I_28^m, fluid B is a mixture of C_4H_{10} and C_3H_8, and the volume fractions of C_4H_{10} and C_3H_8 are 59.80 % and 40.20 %. In cases I_21–I_23 and I_29^m–I_215^m, fluid B is SF_6, and fluid A is the artificial gas whose ρ_A and γ_A are determined by (2.5) to satisfy the total transmission condition. The units of L_0 (L_0^m), λ, a_1^0 and a_2^0 are mm, the unit of ΔU is m s^{-1} and the unit of ρ_A and ρ_B is kg m^{-3}.

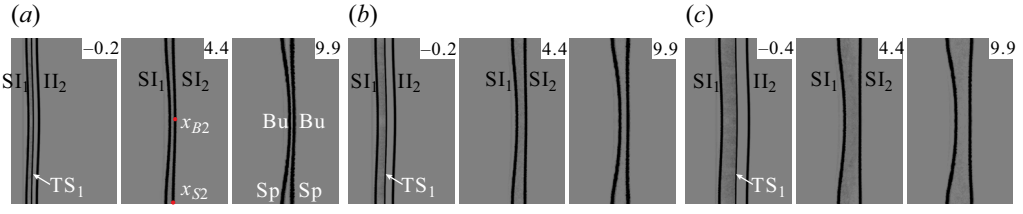

Figure 9. Numerical schlieren images of the shocked heavy fluid layer for cases I_21 (*a*), I_22 (*b*) and I_23 (*c*). Here, 'x_{B2}' and 'x_{S2}' denote the tips of bubbles and spikes for the second interface, respectively. Numbers denote the dimensionless time $k\Delta U(t - t^*)$.

with cases I_24^m–I_28^m, their amplitude growth data are correspondingly higher. Overall, the second interface's amplitude growths are roughly frozen for all of these cases, indicating that both (2.23) and (2.27) are necessary to achieve freeze-out for the second interface. Additionally, apart from the limitation of L_0^m, the model (2.23) is insensitive to variations in M_s, R_0, λ and gas species.

In short, the smaller value of a_2^0 determined by our freeze-out theory compared with the value of a_1^0 (see table 2) results in a lower-amplitude growth rate for the second interface. As a result, the bubble of the first interface more effectively squeezes the counterpart of the second interface, preventing the second interface's phase reversal when $L_0 < L_0^m$ and thereby leading to freeze-out for the second interface.

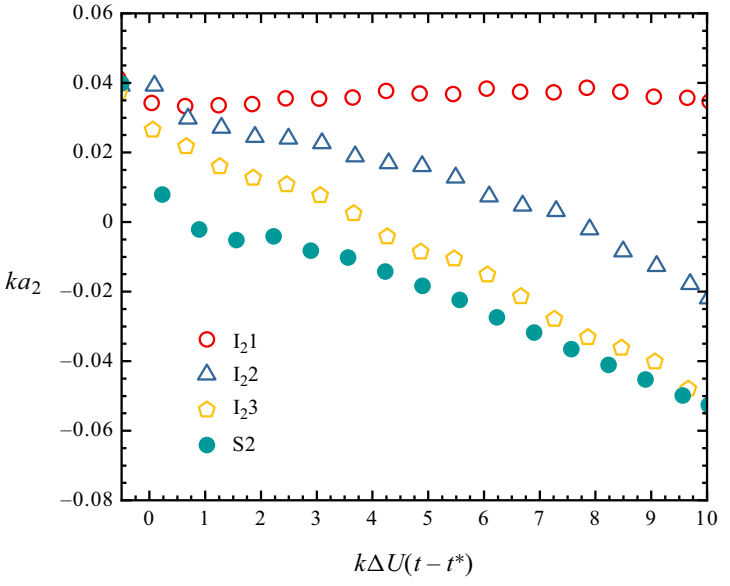

Figure 10. Time variations of the second interface's amplitudes for cases I_21–I_23 in a dimensionless form. Case S2 is a single-mode case included for comparison.

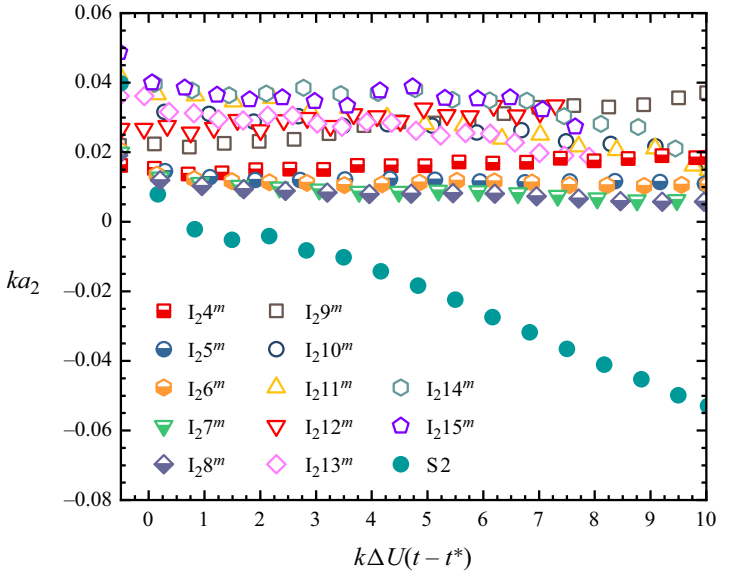

Figure 11. Time variations of the second interface's amplitudes for cases I_24^m–I_215^m in a dimensionless form.

5. Examination of freeze-out for double interfaces and for the fluid-layer width growth

In this section, we will first explore the feasibility of achieving simultaneous freeze-out for both the first and second interfaces. Notably, the models (2.22) and (2.23) are insufficient for predicting the simultaneous freeze-out for double interfaces as these two equations

Case	M_s	L_0	R_0	λ	a_1^0	a_2^0	$\sin\theta^*$	ΔU	ρ_A	γ_A	ρ_B	γ_B
DI1-*a*, *b*, *c*, *d*	2.0	28.7	3	120	1.0	1.69, 0.76, 1.0, 1.1	0.615	254.8	2.03	4.72	6.08	1.10
DI2-*a*, *b*, *c*, *d*	2.0	10	3	120	1.0	0.9, 1.0, 1.1, 1.2	0.655	254.8	2.03	4.72	6.08	1.10
DI3	2.0	10	2	120	1.0	1.1	0.647	239.4	3.04	2.89	6.08	1.10
DI4	2.0	10	4	120	1.0	1.1	0.658	262.4	1.52	6.56	6.08	1.10
DI5	1.2	10	3	120	1.0	1.1	0.589	66.5	2.03	3.81	6.08	1.10
DI6	1.6	10	3	120	1.0	1.1	0.645	169.2	2.03	4.41	6.08	1.10

Table 3. Initial conditions of cases designed for testing freeze-out for double interfaces and for fluid-layer width growth. The units of L_0, λ, a_1^0 and a_2^0 are mm, the unit of ΔU is $\mathrm{m\,s^{-1}}$ and the unit of ρ_A and ρ_B is $\mathrm{kg\,m^{-3}}$.

cannot hold concurrently. Nevertheless, these equations still offer valuable insights into the simultaneous freeze-out. Specifically, after setting an initial amplitude (a_1^0) for the first interface, we can determine the initial amplitudes of the second interface based on (2.22) and (2.23), denoted as a_2^{01} and a_2^{02}, which correspond to the requirements for individual freeze-out for the first and second interfaces, respectively. Notably, in the scenarios with a_2^{01} or a_2^{02}, the amplitude growth of one interface has been confirmed to be frozen, as demonstrated in § 4.2 or § 4.3. However, it remains unclear whether the amplitude growth of the other interface is frozen. Even if the freeze-out for the other interface is not achieved, a_2^{01} and a_2^{02} would establish the upper and lower bounds in our search for a suitable a_2^0 for the simultaneous freeze-out case. When a_1^0 is fixed, our freeze-out theory gives a larger a_2^{01} and a smaller a_2^{02}, i.e. the inequality $a_2^{01} > a_1^0 > a_2^{02}$ holds. In the range of a_2^{01} to a_2^{02}, we can identify a value for a_2^0 that may be valid for simultaneous freeze-out of double interfaces. Particularly, the special scenario of $a_2^0 = a_1^0$ will be examined.

Cases DI1-*a*, DI1-*b* and DI1-*c* are designed, based on the aforementioned analysis, to examine the simultaneous freeze-out for double interfaces. In these cases, a_1^0 is set to 1 mm, and then, a_2^{01} and a_2^{02} are theoretically determined to be 1.69 mm and 0.76 mm. As a result, including the scenario of $a_2^0 = a_1^0$, a_2^0 in the three cases is set to 1.69 mm, 0.76 and 1 mm, respectively. Notably, the freeze-out for the second interface requires L_0 to be no greater than L_0^m. Thus, we first examine the simultaneous freeze-out for double interfaces at $L_0 = L_0^m$, specifically, 28.7 mm. Other initial parameters for cases DI1-*a*, *b*, *c* are listed as follows: M_s, R_0 and λ are 2.0, 3 and 120 mm, respectively; and the heavy fluid is SF_6. Further details about the initial conditions for the three cases are presented in table 3.

Figures 12(*a*), 12(*b*) and 12(*c*) show numerical schlieren images illustrating the interface evolution for cases DI1-*a*, DI1-*b* and DI1-*c*, respectively. These cases exhibit distinct interface morphologies due to different initial amplitudes for the second interface. The interface evolutions for cases DI1-*a* and DI1-*b* are similar to those presented in figures 7(*a*) and 9(*a*), respectively, and are thus not discussed here. For case DI1-*c*, as shown in figure 12(*c*), the second interface completes the phase reversal with time, and at a late moment ($k\Delta Ut = 9.3$), a near-mirror state between the first and second interfaces is observed.

To assess the freeze-out for each interface in cases DI1-*a*, *b*, *c*, the data of dimensionless amplitude growth for the first and second interfaces are plotted in figure 13. In the case of DI1-*a*, the amplitude growth of the first interface is nearly frozen, while the

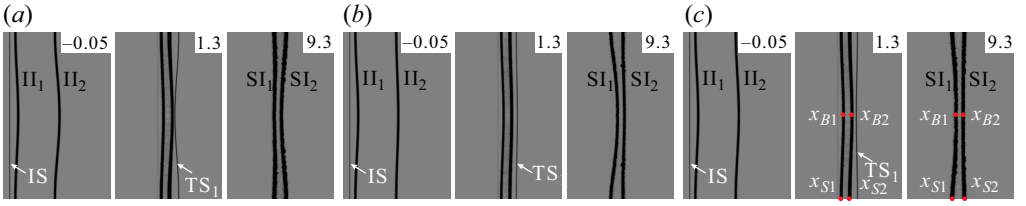

Figure 12. Numerical schlieren images of the shocked heavy fluid layer for cases DI1-*a* (*a*), DI1-*b* (*b*) and DI1-*c* (*c*). Numbers denote the dimensionless time $k\Delta Ut$.

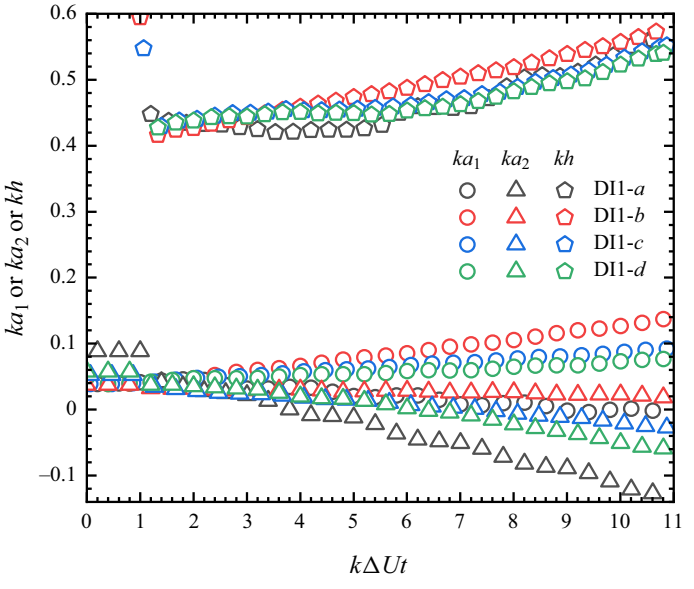

Figure 13. Dimensionless temporal variations of interface amplitudes and fluid-layer widths for cases DI1-*a*, *b*, *c*, *d*. The dashed lines, as auxiliary ones, are plotted to better identify the growth behaviour of the interface amplitude and fluid-layer width, and similarly hereinafter.

second interface exhibits continuous negative amplitude growth. For case DI1-*b*, the amplitude growth of the second interface is almost stagnant, whereas the amplitude of the first interface grows rapidly. These behaviours indicate that the simultaneous freeze-out for both the first and second interfaces is infeasible, because the freeze-out for one interface requires the other interface to have a higher initial amplitude (i.e. a greater amplitude growth rate), leading to an inherent inability to freeze the amplitude growth of the other interface. In case DI1-*c*, the amplitude growth for both interfaces is not stagnant, falling between the amplitude growth of cases DI1-*a* and DI1-*b*. This indicates that, when the difference in amplitude growth rates between the first and second interfaces is not sufficiently large, the amplitude growth for both interfaces cannot be frozen.

We turn our attention to the freeze-out of the whole fluid-layer width growth, given that the simultaneous freeze-out of amplitude growth for both the first and second interfaces is infeasible. The fluid-layer width (h) is defined as the distance between the leftmost and rightmost sides of the fluid layer. Notably, the measurement position for h is different before and after the accomplishment of phase reversal for an interface. Taking case

DI1-*c* as an illustrative example, as presented in figure 12(*c*), $h = x_{B2} - x_{S1}$ before the second interface's phase reversal; and $h = x_{S2} - x_{S1}$ after the second interface's phase reversal.

The dimensionless temporal evolution of the fluid-layer width for cases DI1-*a*, *b*, *c* is presented in figure 13. Disregarding the shock-compression stage ($k\Delta Ut < 1.2$), the fluid-layer width for case DI1-*a* experiences a slight decrease prior to the second interface's phase reversal ($k\Delta Ut < 4.0$). However, after the phase reversal, the fluid-layer width for case DI1-*a* undergoes a rapid increase. In the case of DI1-*b*, the persistent amplitude growth of the first interface leads to a continuous increase in the fluid-layer width. These behaviours indicate that both selections of a_2^{01} and a_2^{02} are invalid for freezing the fluid-layer width growth due to the rapid amplitude growth of one of the fluid-layer interfaces. In case DI1-*c*, when $1 < k\Delta Ut < 5$, the fluid-layer width exhibits slow growth; however, after the second interface's phase reversal ($k\Delta Ut > 7.5$), the fluid-layer width grows rapidly. Notably, during the interval of $5 < k\Delta Ut < 7.5$, although the second interface does not accomplish the phase reversal, the fluid-layer width increases relatively rapidly, primarily attributed to the comparatively fast amplitude growth of the first interface during this period.

A supplementary case, DI1-*d* (see table 3 for details of this case), is examined, featuring a slightly higher a_2^0 ($= 1.1\ mm$) compared with a_1^0. This case is designed to suppress the amplitude growth for the first interface, and thus to facilitate freeze-out of the fluid-layer width growth. The temporal variations of interface amplitudes and fluid-layer widths for case DI1-*d* are presented in figure 13. One can find that the amplitude growth for the first interface in case DI1-*d* is mildly suppressed so that the stagnation of fluid-layer width growth lasts almost until the moment when the second interface completes phase reversal ($k\Delta Ut \approx 7$).

It is evident that the second interface's phase reversal is the main reason why the fluid-layer width growth cannot be frozen. In later examinations, the initial layer thickness is reduced from L_0^m (28.7 mm) to approximately $L_0^m/3$ (10 mm). This adjustment results in an increase in interface coupling strength ($\sin\theta^*$ increases from 0.615 to 0.655, approaching the maximum value of 2/3), which may be helpful for the prevention of the second interface's phase reversal. Four cases of DI2-*a*, *b*, *c*, *d* are designed for further examination. In these cases, a_1^0 is consistently set to 1 mm, whereas a_2^0 is set to 0.9 mm, 1.0 mm, 1.1 mm and 1.2 mm, respectively. All values of a_2^0 fall between a_1^{01} and a_1^{02} determined by our freeze-out theory. Further details of initial conditions for cases DI2-*a*, *b*, *c*, *d* are provided in table 3.

Figure 14 illustrates the dimensionless temporal variations of interface amplitudes and fluid-layer widths for cases DI2-*a*, *b*, *c*, *d*. One can find that, among the four cases, case DI2-*b*, featuring a slightly higher a_2^0 ($= 1.1\ mm$) compared with a_1^0, offers the most favourable condition for the freeze-out of fluid-layer width growth, which is similar to the finding in figure 13. Unfortunately, this freeze-out state is still disrupted after the second interface's phase reversal.

Furthermore, cases DI3–DI4 and DI5–DI6, considering variations in R_0 and M_s, respectively, are designed to examine the setting of a slightly larger a_2^0. In these cases, $a_1^0 = 1$ mm, $a_2^0 = 1.1$ mm and $L_0 = 10$ mm. Further details of initial conditions for these cases are summarized in table 3. Figure 15 presents the temporal variations of interface amplitudes and fluid-layer widths for cases DI3–DI6, respectively. It is observed that, for all four cases, the fluid-layer width growth remains nearly stagnant before the second interface's phase reversal.

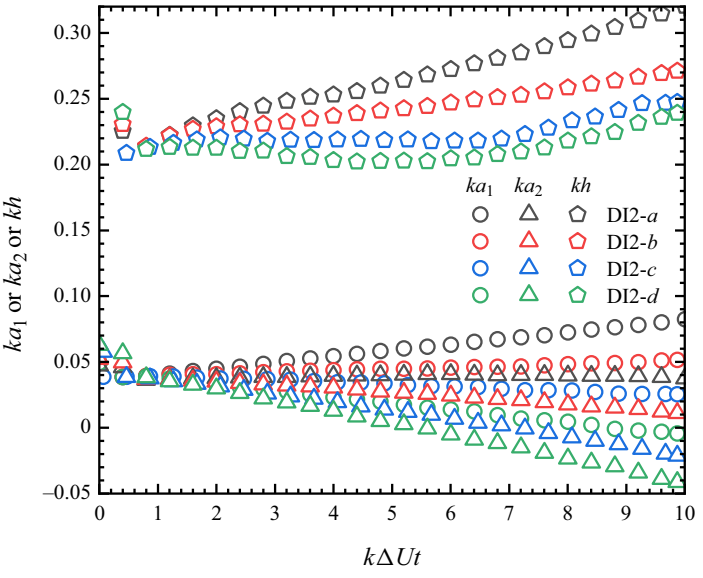

Figure 14. Dimensionless temporal variations of interface amplitudes and fluid-layer widths for cases DI2-a, b, c, d.

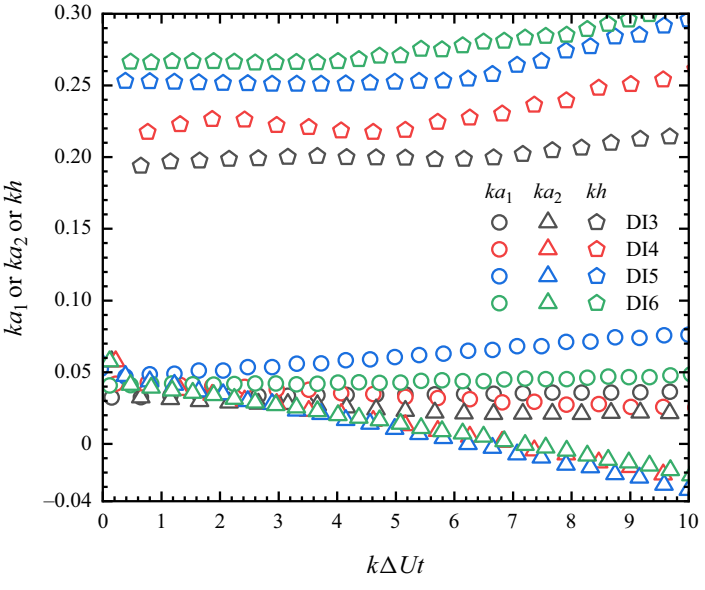

Figure 15. Dimensionless temporal variations of interface amplitudes and fluid-layer widths for cases DI3–DI6. Note that the data for the dimensionless fluid-layer width (kh) in case DI5 are scaled by a factor of 0.6.

In short, the setting of a slightly higher a_2^0 can mildly impede the amplitude growth for the first interface, favouring the freeze-out of fluid-layer width growth over a relatively long time. However, this setting makes it infeasible to prevent the phase reversal at the second interface, ultimately leading to the destruction of freeze-out for the fluid-layer width growth after the second interface's phase reversal.

6. Conclusions

Freeze-out of perturbation growth for heavy fluid layers is investigated both theoretically and numerically. To achieve freeze-out, reverberating waves, generated by interactions between the shock and the fluid layer, are eliminated using specific flow conditions determined through shock dynamics theories. A theoretical model is developed to predict freeze-out for the fluid-layer interfaces. A compressible flow solver, capable of simultaneously capturing discontinuities (such as shock wave and material interface) and resolving small-scale smooth structures, is employed to simulate the freeze-out scenario involving the shock–layer interaction. Overall, the individual freeze-out for the first and second interfaces, as well as the freeze-out of the whole fluid-layer width growth, is achieved.

Physically, to achieve the freeze-out for the first interface, a higher initial amplitude of the second interface is required. This causes a higher initial amplitude growth rate for the second interface, effectively squeezing the first interface's bubble and thus inhibiting the interface evolution. Conversely, to achieve the freeze-out for the second interface, a higher initial amplitude of the first interface and a relatively small initial layer thickness are necessary to prevent the phase reversal of the second interface. Since the freeze-out for one interface requires the other interface to have a higher initial amplitude, the freeze-out conditions for the two interfaces cannot be satisfied simultaneously. In other words, the simultaneous freeze-out of both the first and second interfaces is infeasible. By setting a slightly larger initial amplitude for the second interface to mildly inhibit the amplitude growth of the first interface, the whole fluid-layer width growth is effectively arrested before the second interface's phase reversal.

Theoretically, the individual freeze-outs for the first and second interfaces are predicted. First, by revising the model of Mikaelian (1995) with reasonable post-shock quantities, a theory is established to quantify the parameters required for freeze-out, including the initial amplitudes of the first and second interfaces and the interface coupling strength. Then, a model, as the supplementary condition for the second interface's freeze-out is developed to characterize the maximum initial layer thickness, which prevents the second interface's phase reversal. When the initial layer thickness is below this threshold, the freeze-out of the second interface becomes feasible. The effectiveness of the theory in predicting individual freeze-outs of the first and second interfaces is validated numerically over a broad range of initial conditions.

These findings enhance our understanding of suppressing interfacial instabilities in ICF. Moreover, the theory developed in this work may remain effective in predicting freeze-out for a light fluid layer, which is more relevant to double-shell implosion in ICF. In a following work, this will be examined.

Funding. This work was supported by the National Natural Science Foundation of China (nos. 12302371, 12027801 and 12388101) and the Fundamental Research Funds for the Central Universities (no. WK2090000048).

Declaration of interests. The authors report no conflict of interest.

Author ORCIDs.
Xu Guo https://orcid.org/0000-0002-1280-4968;
Wan Cheng https://orcid.org/0000-0003-3960-4162;
Ting Si https://orcid.org/0000-0001-9071-8646.

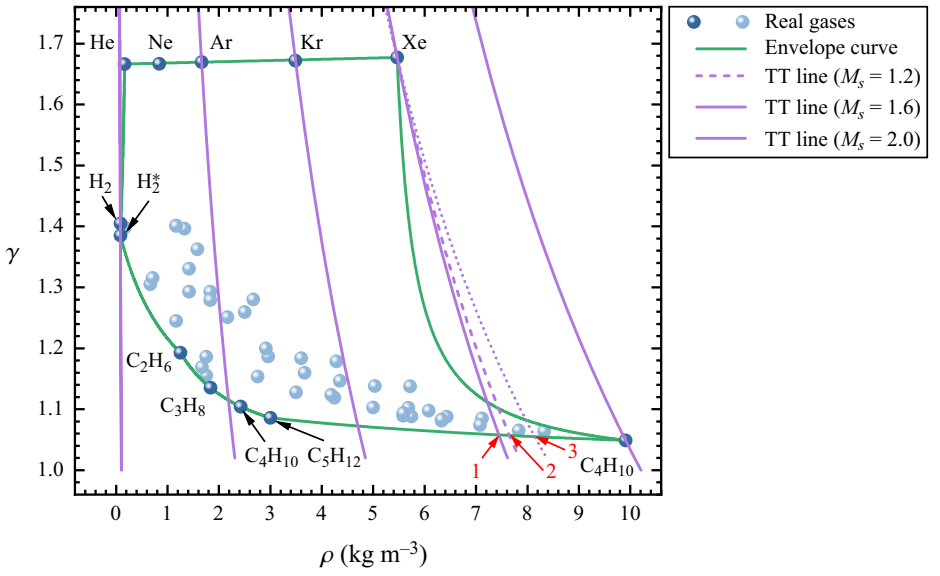

Figure 16. The ρ–γ plot for 56 real gases. The envelope curve represents the limit of ρ and γ achievable by real gases and their mixtures. The TT line denotes the total transmission line. By selecting any two gases from the TT line as fluids A and B on both sides of an interface, total transmission can be achieved.

Gas	Formula	ρ (kg m^{-3})	γ	C_p (J mol^{-1} K^{-1})	C_v (J mol^{-1} K^{-1})
Hydrogen	H_2	0.084	1.405	28.85	20.53
Parahydrogen	H_2 *	0.084	1.385	29.93	21.61
Helium	He	0.17	1.666	20.79	12.47
Neon	Ne	0.84	1.667	20.79	12.47
Ethane	C_2H_6	1.25	1.193	53.05	44.48
Argon	Ar	1.66	1.670	20.83	12.48
Propane	C_3H_8	1.84	1.135	74.63	65.72
Butane	C_4H_{10}	2.42	1.104	101.06	91.51
Neopentane	C_5H_{12}	3.00	1.086	124.32	114.48
Krypton	Kr	3.49	1.672	20.88	12.49
Xenon	Xe	5.47	1.677	21.01	12.53
Decafluorobutane	C_4F_{10}	9.91	1.049	207.61	197.91

Table 4. Properties of the 12 gases on the envelope curve in figure 16. Here, C_p (C_v) are the specific heat at constant pressure (volume). Here, $\gamma = C_p/C_v$. The formulas represented by (·) and (·)* indicate structural isomers of each other.

Appendix A. Total transmission under real-gas conditions

Figure 16 shows the ρ–γ plot for 56 real gases that exist under normal temperature and pressure conditions (in this work, at 295 K and 101.3 kPa). The details of these 56 real gases are provided in tables 4 and 5. It is found that H_2 has the smallest density, while decafluorobutane (C_4F_{10}) has the largest; C_4F_{10} has the smallest adiabatic index, whereas Xe has the largest. For all real gases, the density (ρ) varies from 0.084 to 9.91 kg m^{-3}, and the adiabatic index (γ) varies from 1.049 to 1.677.

The total transmission imposes strict criteria on the density and adiabatic index of the gases. To fulfil these requirements, we can generate a gas mixture by blending two distinct

Gas	Formula	ρ (kg m^{-3})	γ	Gas	Formula	ρ (kg m^{-3})	γ
Deuterium	D_2	0.17	1.398	R143a	$C_2H_3F_3$	3.50	1.128
Methane	CH_4	0.67	1.305	R22	$CHClF_2$	3.60	1.184
Ammonia	NH_3	0.71	1.316	R14	CF_4	3.66	1.160
Carbon monoxide	CO	1.17	1.401	R142b	$C_2H_3ClF_2$	4.18	1.124
Nitrogen	N_2	1.17	1.401	R134a	$C_2H_2F_4$	4.25	1.119
Ethene	C_2H_4	1.17	1.245	R21	$CHCl_2F$	4.28	1.179
Oxygen	O_2	1.33	1.396	R13	$CClF_3$	4.35	1.147
R41	CH_3F	1.42	1.293	R125	C_2HF_5	5.00	1.103
Hydrogen sulphide	H_2S	1.42	1.331	R12	CCl_2F_2	5.03	1.138
Fluorine	F_2	1.58	1.363	R245ca	$C_3H_3F_5$	5.58	1.089
Propyne	C_3H_4	1.67	1.169	R245fa	$C_3H_3F_5$ *	5.58	1.093
Propene	C_3H_6	1.75	1.156	R124	C_2HClF_4	5.68	1.103
Cyclopropane	C_3H_6 *	1.75	1.186	R11	CCl_3F	5.72	1.138
Carbon dioxide	CO_2	1.83	1.293	R116	C_2F_6	5.75	1.089
Dinitrogen monoxide	N_2O	1.83	1.280	Sulphur hexafluoride	SF_6	6.08	1.098
R32	CH_2F_2	2.17	1.251	R236ea	$C_3H_2F_6$	6.33	1.081
Isobutane	C_4H_{10} *	2.42	1.104	R236fa	$C_3H_2F_6$ *	6.33	1.083
Carbonyl sulphide	COS	2.50	1.260	R115	C_2ClF_5	6.43	1.088
Sulphur dioxide	SO_2	2.67	1.280	R227ea	C_3HF_7	7.08	1.074
R152a	$C_2H_4F_2$	2.75	1.154	R114	$C_2Cl_2F_4$	7.12	1.085
R23	CHF_3	2.91	1.200	R218	C_3F_8	7.83	1.066
Nitrogen trifluoride	NF_3	2.96	1.187	RC318	C_4F_8	8.33	1.064

Table 5. Properties of the 44 gases within the envelope curve in figure 16. The formulas represented by (·) and (·)* indicate structural isomers of each other. Notably, isobutane (C_4H_{10} *) is the structural isomer of butane (C_4H_{10}) presented in table 4.

gases. The density (ρ_{mix}) and adiabatic index (γ_{mix}) of the gas mixture can be expressed as follows:

$$\rho_{mix} = (1-\epsilon)\rho_1 + \epsilon\rho_2, \tag{A1}$$

$$\gamma_{mix} = \frac{\gamma_1(\gamma_2-1)+\epsilon(\gamma_1-\gamma_2)}{\gamma_2-1+\epsilon(\gamma_1-\gamma_2)}, \tag{A2}$$

where ρ_1 (γ_1) and ρ_2 (γ_2) denote the densities (adiabatic indices) of gas 1 and gas 2, respectively; the parameter $\epsilon \in (0, 1)$ denotes the volume fraction. Using the example of two gases, Kr and Xe, we can vary the value of ϵ from 0 to 1, generating the theoretical ρ–γ curve denoted by the green line between the data points of Kr and Xe in figure 16. This line represents the ensemble of density and adiabatic index for the gas mixture obtained by mixing Kr and Xe in various proportions. Furthermore, by mixing the two neighbouring gases among the outermost 12 gases (see table 4 for details) denoted by dark blue symbols in figure 14, we can derive the theoretical ρ–γ envelope curve, depicted as the closed green line. The envelope curve represents the limit of ρ and γ achievable by the real gases and their mixtures. The remaining 44 gases (see table 5 for details), indicated by light blue symbols, are within the envelope curve. Moreover, the values of ρ and γ at any point within the envelope curve can be determined by mixing three gases: the two real gases located on the envelope curve and one real gas from within the envelope curve.

Utilizing real gases, we explore the maximum attainable R_0 (R_0^{max}) under the total transmission condition. Taking $M_s = 2.0$ as an example, several total transmission (TT) lines denoted by purple curves are presented in figure 16. By selecting any two gases from

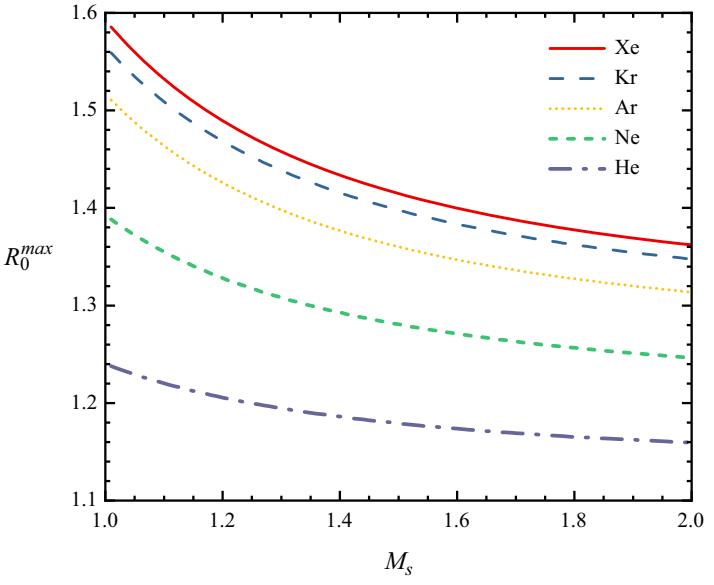

Figure 17. Variations of R_0^{max} vs M_s under total transmission conditions formed by real gases.

a TT line as fluids A and B on both sides of the interface, TT can be achieved. As shown in figure 16, the TT lines become increasingly inclined from left to right. This indicates that to achieve a larger R_0, one should select the two gases represented by the intersections of the TT line with the uppermost and lowermost portions of the envelope curve; and the further to the right the TT line, the more conducive it is to achieving a larger R_0. For the A/B/A-type heavy fluid layer generated by real gases, the R_0^{max} under TT conditions occurs in this case: Xe is selected as fluid A, and the gas determined by the intersection of the TT line passing through the Xe point with the lowermost envelope curve is selected as fluid B. Specifically, at $M_s = 2.0$, 1.6 and 1.2, fluid B corresponds to the gases represented by points 1, 2 and 3, as illustrated in figure 16. In these three cases, R_0^{max} is determined to be 1.36, 1.40 and 1.49, respectively.

To further investigate the relationship between R_0^{max} and M_s, figure 17 presents the M_s–R_0^{max} curves for five typical cases. In these cases, the five gases, He, Ne, Ar, Kr and Xe, are respectively selected as fluid A, and the gases corresponding to the intersections of the TT lines passing through the points of these five gases with the lowermost envelope curve are respectively selected as fluid B. As illustrated in figure 17, as the value of M_s increases, the value of R_0^{max} decreases.

References

Abgrall, R. & Karni, S. 2001 Computations of compressible multifluids. *J. Comput. Phys.* **169**, 594–623.

Balakumar, B.J., Orlicz, G.C., Ristorcelli, J.R., Balasubramanian, S., Prestridge, K.P. & Tomkins, C.D. 2012 Turbulent mixing in a Richtmyer–Meshkov fluid layer after reshock: velocity and density statistics. *J. Fluid Mech.* **696**, 67–93.

Balakumar, B.J., Orlicz, G.C., Tomkins, C.D. & Prestridge, K.P. 2008 Simultaneous particle-image velocimetry-planar laser-induced fluorescence measurements of Richtmyer–Meshkov instability growth in a gas curtain with and without reshock. *Phys. Fluids* **20**, 124103.

Balasubramanian, S., Orlicz, G.C. & Prestridge, K.P. 2013 Experimental study of initial condition dependence on turbulent mixing in shock-accelerated Richtmyer–Meshkov fluid layers. *J. Turbul.* **14**, 170–196.

BETTI, R. & HURRICANE, O.A. 2016 Inertial-confinement fusion with lasers. *Nat. Phys.* **12**, 435–448.
CHARAKHCH'YAN, A.A. 2000 Richtmyer–Meshkov instability of an interface between two media due to passage of two successive shocks. *J. Appl. Mech. Tech. Phys.* **41**, 23–31.
CHARAKHCH'YAN, A.A. 2001 Reshocking at the non-linear stage of Richtmyer–Meshkov instability. *Plasma Phys. Control. Fusion* **43**, 1169.
CHEN, C., WANG, H., ZHAI, Z. & LUO, X. 2023*a* Attenuation of perturbation growth of single-mode SF_6–air interface through reflected rarefaction waves. *J. Fluid Mech.* **969**, R1.
CHEN, C., XING, Y., WANG, H., ZHAI, Z. & LUO, X. 2023*b* Freeze-out of perturbation growth of single-mode helium-air interface through reflected shock in Richtmyer–Meshkov flows. *J. Fluid Mech.* **956**, R2.
CONG, Z., GUO, X., SI, T. & LUO, X. 2022 Experimental and theoretical studies on heavy fluid layers with reshock. *Phys. Fluids* **34**, 104108.
DESJARDINS, T.R., *et al.* 2019 A platform for thin-layer Richtmyer–Meshkov at OMEGA and the NIF. *High Energy Density Phys.* **33**, 100705.
GLENDINNING, S.G., *et al.* 2003 Effect of shock proximity on Richtmyer–Meshkov growth. *Phys. Plasmas* **10**, 1931–1936.
GUO, X., CONG, Z., SI, T. & LUO, X. 2022*a* Shock-tube studies of single- and quasi-single-mode perturbation growth in Richtmyer–Meshkov flows with reshock. *J. Fluid Mech.* **941**, A65.
GUO, X., SI, T., ZHAI, Z. & LUO, X. 2022*b* Large-amplitude effects on interface perturbation growth in Richtmyer–Meshkov flows with reshock. *Phys. Fluids* **34**, 082118.
GUO, X., ZHAI, Z., DING, J., SI, T. & LUO, X. 2020 Effects of transverse shock waves on early evolution of multi-mode chevron interface. *Phys. Fluids* **32**, 106101.
HAN, Z. & YIN, X. 1993 *Shock Dynamics*. Kluwer Academic.
HOLMES, R.L., DIMONTE, G., FRYXELL, B., GITTINGS, M.L., GROVE, J.W., SCHNEIDER, M., SHARP, D.H., VELIKOVICH, A.L., WEAVER, R.P. & ZHANG, Q. 1999 Richtmyer–Meshkov instability growth: experiment, simulation and theory. *J. Fluid Mech.* **389**, 55–79.
JACOBS, J.W., JENKINS, D.G., KLEIN, D.L. & BENJAMIN, R.F. 1995 Nonlinear growth of the shock-accelerated instability of a thin fluid layer. *J. Fluid Mech.* **295**, 23–42.
JACOBS, J.W., KLEIN, D.L., JENKINS, D.G. & BENJAMIN, R.F. 1993 Instability growth patterns of a shock-accelerated thin fluid layer. *Phys. Rev. Lett.* **70**, 583–586.
KURANZ, C.C, PARK, H.-S., HUNTINGTON, C.M., MILES, A.R., REMINGTON, B.A., PLEWA, T., TRANTHAM, M.R., ROBEY, H.F., SHVARTS, D. & SHIMONY, A. 2018 How high energy fluxes may affect Rayleigh–Taylor instability growth in young supernova remnants. *Nat. commun.* **9**, 1–6.
LI, J., CAO, Q., WANG, H., ZHAI, Z. & LUO, X. 2023 New interface formation method for shock-interface interaction studies. *Exp. Fluids* **64**, 170.
LIANG, Y., LIU, L., ZHAI, Z., SI, T. & WEN, C. 2020 Evolution of shock-accelerated heavy gas layer. *J. Fluid Mech.* **886**, A7.
LIANG, Y. & LUO, X. 2023 Hydrodynamic instabilities of two successive slow/fast interfaces induced by a weak shock. *J. Fluid Mech.* **955**, A40.
LINDL, J., LANDEN, O., EDWARDS, J., MOSES, E. & TEAM, N. 2014 Review of the National Ignition Campaign 2009–2012. *Phys. Plasmas* **21**, 020501.
LOMBARDINI, M. & PULLIN, D.I. 2009 Startup process in the Richtmyer–Meshkov instability. *Phys. Fluids* **21**, 297–372.
MESHKOV, E.E. 1969 Instability of the interface of two gases accelerated by a shock wave. *Fluid Dyn.* **4**, 101–104.
MEYER, K.A. & BLEWETT, P.J. 1972 Numerical investigation of the stability of a shock-accelerated interface between two fluids. *Phys. Fluids* **15**, 753–759.
MIKAELIAN, K.O. 1983 Time evolution of density perturbations in accelerating stratified fluids. *Phys. Rev.* A **28**, 1637–1646.
MIKAELIAN, K.O. 1985 Richtmyer–Meshkov instabilities in stratified fluids. *Phys. Rev.* A **31**, 410–419.
MIKAELIAN, K.O. 1994 Freeze-out and the effect of compressibility in the Richtmyer–Meshkov instability. *Phys. Fluids* **6**, 356–368.
MIKAELIAN, K.O. 1995 Rayleigh–Taylor and Richtmyer–Meshkov instabilities in finite-thickness fluid layers. *Phys. Fluids* **7**, 888–890.
MIKAELIAN, K.O. 1996 Numerical simulations of Richtmyer–Meshkov instabilities in finite-thickness fluid layers. *Phys. Fluids* **8**, 1269–1292.
MIKAELIAN, K.O. 2010 Analytic approach to nonlinear hydrodynamic instabilities driven by time-dependent accelerations. *Phys. Rev.* E **81**, 016325.
MONTGOMERY, D.S., *et al.* 2018 Design considerations for indirectly driven double shell capsules. *Phys. Plasmas* **25**, 092706.

MOTL, B., OAKLEY, J., RANJAN, D., WEBER, C., ANDERSON, M. & BONAZZA, R. 2009 Experimental validation of a Richtmyer–Meshkov scaling law over large density ratio and shock strength ranges. *Phys. Fluids* **21**, 126102.

ORLICZ, G.C., BALASUBRAMANIAN, S., VOROBIEFF, P. & PRESTRIDGE, K.P. 2015 Mixing transition in a shocked variable-density flow. *Phys. Fluids* **27**, 114102.

RICHTMYER, R.D. 1960 Taylor instability in shock acceleration of compressible fluids. *Commun. Pure Appl. Maths* **13**, 297–319.

SADOT, O., RIKANATI, A., ORON, D., BEN-DOR, G. & SHVARTS, D. 2003 An experimental study of the high Mach number and high initial-amplitude effects on the evolution of the single-mode Richtmyer–Meshkov instability. *Laser Part. Beams* **21**, 341–346.

SAMTANEY, R. & ZABUSKY, N.J. 1994 Circulation deposition on shock-accelerated planar and curved density-stratified interfaces: models and scalling laws. *J. Fluid Mech.* **269**, 45–78.

TAYLOR, G.I. 1950 The instability of liquid surfaces when accelerated in a direction perpendicular to their planes. I. *Proc. R. Soc. Lond.* A **201**, 192–196.

TERRY, M.R., PERKINS, L.J. & SEPKE, S.M. 2012 Design of a deuterium and tritium-ablator shock ignition target for the National Ignition Facility. *Phys. Plasmas* **19**, 112705.

YANG, Q., CHANG, J. & BAO, W. 2014 Richtmyer–Meshkov instability induced mixing enhancement in the scramjet combustor with a central strut. *Adv. Mech. Engng* **6**, 614189.

ZHAI, Z., DONG, P., SI, T. & LUO, X. 2016 The Richtmyer–Meshkov instability of a 'V' shaped air/helium interface subjected to a weak shock. *Phys. Fluids* **28**, 082104.

ZHANG, Y., ZHOU, Z., DING, J. & LUO, X. 2022 Interaction of a planar shock wave with two heavy/light interfaces. *Acta Mech. Sin.* **38**, 322047.

ZHOU, Y. 2017*a* Rayleigh–Taylor and Richtmyer–Meshkov instability induced flow, turbulence, and mixing. I. *Phys. Rep.* **720–722**, 1–136.

ZHOU, Y. 2017*b* Rayleigh–Taylor and Richtmyer–Meshkov instability induced flow, turbulence, and mixing. II. *Phys. Rep.* **723–725**, 1–160.

ZHOU, Y., *et al.* 2021 Rayleigh–Taylor and Richtmyer–Meshkov instabilities: a journey through scales. *Physica* D **423**, 132838.

ZHOU, Z., DING, J., CHENG, W. & LUO, X. 2023*a* Scaling law of structure function of Richtmyer–Meshkov turbulence. *J. Fluid Mech.* **972**, A18.

ZHOU, Z., DING, J., HUANG, S. & LUO, X. 2023*b* A new type of weighted compact nonlinear scheme with minimum dispersion and adaptive dissipation for compressible flows. *Comput. Fluids* **262**, 105934.